Geoenvironmental Disasters

METHODOLOGY Open Access

Adapting sudden landslide identification product (SLIP) and detecting real-time increased precipitation (DRIP) algorithms to map rainfall-triggered landslides in Western Cameroon highlands (Central-Africa)

Alfred Homère Ngandam Mfondoum[1,2*], Pauline Wokwenmendam Nguet[3], Jean Valery Mefire Mfondoum[4], Mesmin Tchindjang[2], Sofia Hakdaoui[5], Ryan Cooper[6], Paul Gérard Gbetkom[7], Joseph Penaye[3], Ateba Bekoa[3] and Cyriel Moudioh[3]

Abstract

Background: NASA's developers recently proposed the Sudden Landslide Identification Product (SLIP) and Detecting Real-Time Increased Precipitation (DRIP) algorithms. This double method uses Landsat 8 satellite images and daily rainfall data for a real-time mapping of this geohazard. This study adapts the processing to face the issues of data quality and unavailability/gaps for the mapping of the recent landslide events in west-Cameroon's highlands.

Methods: The SLIP algorithm is adapted, by integrating the inverse Normalized Difference Vegetation Index (NDVI) to assess the soil bareness, the Modified Normalized Multi-Band Drought Index (MNMDI) combined with the hydrothermal index to assess soil moisture, and the slope inclination to map the recent landslide. Further, the DRIP algorithm uses the mean daily rainfall to assess the thresholds corresponding to the recent landslide events. Their probability density function (PDF) curves are superimposed and their intersections are used to propose sets of dichotomous variables before (1948–2018) and after the 28 October 2019 landslide event. In addition, a survival analysis is performed to correlate landslide occurrence to rainfall, with the first known event in Cameroon as starting point, and using the Cox model.

Results: From the SLIP model, the Landslide Hazard Zonation (LHZ) map gives an overall accuracy of *96%*. Further, the DRIP model states that 6/9 ranges of probability are rainfall-triggered landslides at *99.99%*, between June and October, while 3/9 ranges show only *4.88%* of risk for the same interval. Finally, the survival probability for a known site is up to *0.68* for the best value and between *0.38* and *0.1* for the lowest value through time.

Conclusions: The proposed approach is an alternative based on data (un)availability, completed by the site's lifetime analysis for a more flexibility in observation and prediction thresholding.

Keywords: SLIP, DRIP, Real-time mapping, Geohazard, West-Cameroon highlands, Rainfall-triggered landslides, Cox model, LHZ

* Correspondence: stats.n.maps.expertise@gmail.com
[1]StatsN'Maps, Private Consulting Firm, Dallas, TX, USA
[2]Department of Geography, University of Yaoundé I, Yaoundé, Cameroon
Full list of author information is available at the end of the article

Background

Landslides are natural events (Varnes, 1958, 1978 & 1984; Brusden, 1984; Crozier, 1986; Hutchinson, 1988; Cruden, 1991; Cruden and Varnes, 1996; Courture, 2011; UNISDR,[1] 2017; USGS*, 2004). However, they may turn into serious geohazards responsible for casualties and economical losses worldwide (Petley, 2012). These include loss of lives and damage to human settlements and natural structures, which present a significant constraint for the development of the zones affected. According to the World Health Organization, landslides affected an estimated 4.8 million people and caused more than 18,000 deaths, between 1998 and 2017.[2] It is admitted that at least 90% of losses related can be avoided if the problem is recognized before the landslide occurrence (Brabb, 1993). Therefore, the mitigation measures require to identify existing landslides, and/or to predict of future events and endangered zones. One main issue is that landslide inventories suffer from underreporting at both regional and global scales (UNISDR, 2017). Even in developed countries, the database of landslide events is usually far from complete. Significant gaps in available information additionally contribute to the shortcomings of the inventories due to the lack of routine global monitoring or cataloging systems, such as those available for hurricanes and earthquakes (Kirschbaum et al. 2009). However, mapping landslide deformation and activity is fundamental for the assessment and reduction of hazards and risks related (Zhao and Lu, 2018). To the measures and sketches that result from fieldwork (Yang et al., 2012 & 2015), Earth Observatory (OE) brings the above view that is complementary to assess or predict the hazard.

Remote sensing data and the geospatial sciences are very powerful tools to study the prevailing causal factors and achieve that goal (Tofani et al., 2013). Their integration leads to a standard tool known as landslide susceptibility mapping used around the world by various researchers (Guzzetti et al., 1999; Van Westen et al., 1999), which helps mapping the areas affected or model the likelihood of future landslides based solely on the intrinsic properties of a site. The susceptibility of a given area to landslides can be determined and depicted using hazard zonation (Lin et al., 2017; Dahal and Dahal, 2017). Recent advances identify two sets of methods for landslide hazard zonation (LHZ), such as heuristic (knowledge-based) and data driven (statistical) approaches (Pardeshi et al., 2013; Roy and Saha, 2019).

The heuristic or qualitative approach relies on the distribution (inventory) analysis through field survey mapping, historical records, satellite images and aerial photo interpretation (Varnes, 1984; Cruden, 1991; Colombo et al., 2005; Guzzetti et al. 2005; Galli et al., 2008). Other researchers use decision-action processes and weighing models, including the analytical hierarchy process (AHP) and its different derivatives (Komac, 2006; Gosh et al. 2011; Kayastha et al., 2013; Wu et al., 2016; Meena et al., 2019). The statistical or quantitative approach include bivariate and multivariate modeling methods to minimize subjectivity (Kanungo et al., 2006). Amongst bivariate methods, weights of evidence model, weighted overlay method, frequency ratio approach, information value method and fuzzy logic method are used (Blahut et al. 2010) (Martha et al., 2013; Preuth, et al., 2010; Lee, 2005; Sarkar et al., 2006; Singh et al., 2011). Multivariate are specifically logistic regression analysis, discriminant analysis, artificial neural network (ANN) method and probabilistic approach (Guzzetti et al., 2005, Wang and Sassa, 2005; Lee et al., 2008; Kanungo et al., 2009; Pradhan and Lee, 2009; Bui et al., 2012; Calvello et al., 2013, Meten et al., 2015; Anbalagan et al., 2015).

Nowadays, the quantitative approach is supported by several machine learning algorithms with better accuracy. They can be single or hybrids, and amongst them are processing such as the support vector machine (SVM), Random Forest (RF), Fisher's Linear Discriminant Analysis (FLDA), Bayesian Network (BN), Logistic Regression (LR), and Naïve Bayes (NB), or more recently the AdaBoost, MultiBoost, Bagging, and Rotation Forest (Marjanovic et al., 2011; Goetz et al., 2015; Pham et al., 2016a & b; Ada and San, 2018; Pham et al., 2018; Shirzadi et al., 2018; Sharma and Mahajan, 2018; Garosi et al., 2018; Cavanesi et al., 2020; Xiao, et al., 2020; Xiong et al., 2020; Nam and Wang, 2020). Both qualitative and quantitative methods keep improving their processes to map and assess the areas affected.

Besides, a novelty approach has recently emerged, ambitioning to fill the methodological voids of landslide monitoring. In a double set of processing, based on the availability of hourly rainfall data and the more recent free satellite images, instantaneous assessment and prediction of landslide events became possible for spatially extended regions thanks to the analytical power and the flexibility of Google Earth Engine platform and tools. The pioneering model was developed in 2019 by a team of NASA's developers (Fayne et al., 2019) and is detailed in the methodology section. This method is known as, the Sudden Landslide Identification Product (SLIP), combined with the Detecting Real-Time Increased Precipitation (DRIP), to simultaneously map the affected surface, as well as identifies intensity and timing of rainfall that had triggered the event.

[1]United Nations Office for Disaster Risk Reduction; *United States Geological Survey.
[2]https://www.who.int/health-topics/landslides#tab=tab_1.

With the advantages of this latter, i.e., the opensource data and the relative flexibility of the method that relies on indices calculation and rainfall sequences, the present study has envisaged to map the rainfall-triggered landslides events in west-Cameroon highlands, based on recent deadly events. Nonetheless, there are several local obstacles to its full implementation, among which three majors: *i)* first of all, free Landsat 8 images covering the area usually have at least 50% cloud cover in permanence, and those less cloudy are unequally distributed in time, thus making impossible an efficient monitoring every 16 days; *ii)* the poor spatial and temporal data availability, due to the insufficient number of stations only present in few main cities, and the lack of hourly records caused by obsolete materials; *iii)* at last, and non the least issue, there is no a detailed and accurate landslide inventory in Cameroon, in terms of date, proper location with geographical coordinates, and statistics on social and economic losses. These lacks and gaps clearly impede the full implementation of the SLIP/DRIP model.

Therefore, this paper proposes a derivative SLIP/DRIP procedure, adapted to countries and world's areas facing the same difficulties above-listed. This alternative fits in this study, Cameroon's local scientific and economic conditions, by finding way-outs for efficient results, adjusting the processing as possible to a context of missing data, and introducing a complementary process of the survival analysis of (potentially) affected sites.

Study location

This study was carried out at a regional scale, on a subset of Cameroon's western highlands (Fig. 1a-c) covering 3930.35 km^2. The area belongs to the Cameroon Volcanic Line (CVL), one of the several segments of the African Plate, oriented NE between 9 and 11° of latitude and SW 5–7° East longitude and forming a horst (Elsheikh et al., 2014; Wokwenmendam Nguet, 2019). It is an area of transition between the Cameroon's rainy and dry areas. Its morphology is complex and consists of high plateaus, volcanic massifs as well as plains or collapse basins corresponding to the graben (Balla et al., 2013). The three main morphological components are the Bamenda Plateau (2200 m), the Bamiléké Plateau (1400 to 1600 m), and the Bamoun Plateau (1000 to 1300 m). Ages of the volcanic products along these edifices range from the *Eocene* to the *Pliocene* periods (Moundi et al., 2007; Moundi et al., 2008; Ngongang et al., 2015). The Noun and Ndop plains are flatted terrain, with average altitudes of 1000 m while the Mbo plain's altitudes range from 700 to 800 m, and there are several volcanic lakes. The geological formations made up of products of volcanic eruptions are lying on a basement rocks of plutono-metamorphic nature, and of Precambrian to Panafrican age (Njilah, 1991; Njonfang et al., 1998; Djouka et al., 2008). These basement rocks are usually associated with basic rocks (amphibolite and monzodiorite) and are masked in some places by a thick volcanic cover.

Annual rainfall increases from 100 mm to more than 3300 mm in the southern part around the city of Bafoussam, and 20 mm to more than 2400 mm when evolving to the northern part around Njimom due to the high altitude (Local agro-meteorology offices, Annual reports). Twelve months average temperature is between 26° and 28° Celsius. The vegetation mixes highlands forest and sub-tropical savannah, depending on the rainfall and the sun exposition. The population is 1,720,047 inhabitants, with a density of 124 inhabitants per km^2.

In addition to the rainfall spatial distribution (Fig. 1d & e), human activities and settlements such as agriculture or buildings, mainly occupy slopes or shallows, exposing populations to natural hazards. For instance, on the 4th and 5th September 2018, terrain cracking followed by blocks slides damaged dozens of houses in the city of Foumban (IGMR-Penaye et al., 2018; Fig. 2a), caused the delocalization of hundreds of inhabitants. More recently, during the night of 27 to 28 October 2019, a long and huge rainfall of about 36 h triggered a rotational to translational landslide in Bafoussam (IGMR-Kankeu & Ntchantcho, 2019; Fig. 2b), the deadliest in that area with 45 deaths, dozens of missing people and at least 100 houses destroyed. Moreover, since the 1950's, more than 136 deaths were recorded in the area (Tchindjang, 2012 & 2013). This context justifies the present research, to support Cameroon's government in anticipating such events and planning efficient mitigation actions.

Methodology

Original steps of SLIP/DRIP methodology

In 2019, National Aeronautics and Space Administration's (NASA) developers proposed the SLIP and DRIP methodology, to automate rainfall-induced landslide identification in Nepal, by using open-source imagery and without the use of proprietary classification software (Fayne et al., 2019). It is a two-sided approach, that uses Landsat-8 imagery satellite imagery data to approximate visible landscape changes, and precipitation data for the landslide event's timing. Python 3 programming language and Google Earth Engine cloud environment support the computations, and the data analysis is based on a spectral band analysis and combined with ancillary field data.

Sudden Landslide Identification Product (SLIP) algorithm takes advantage of spectral properties of vegetation, slope, land-cover type, and soil moisture in biweekly (16 days) time steps to identify the affected area

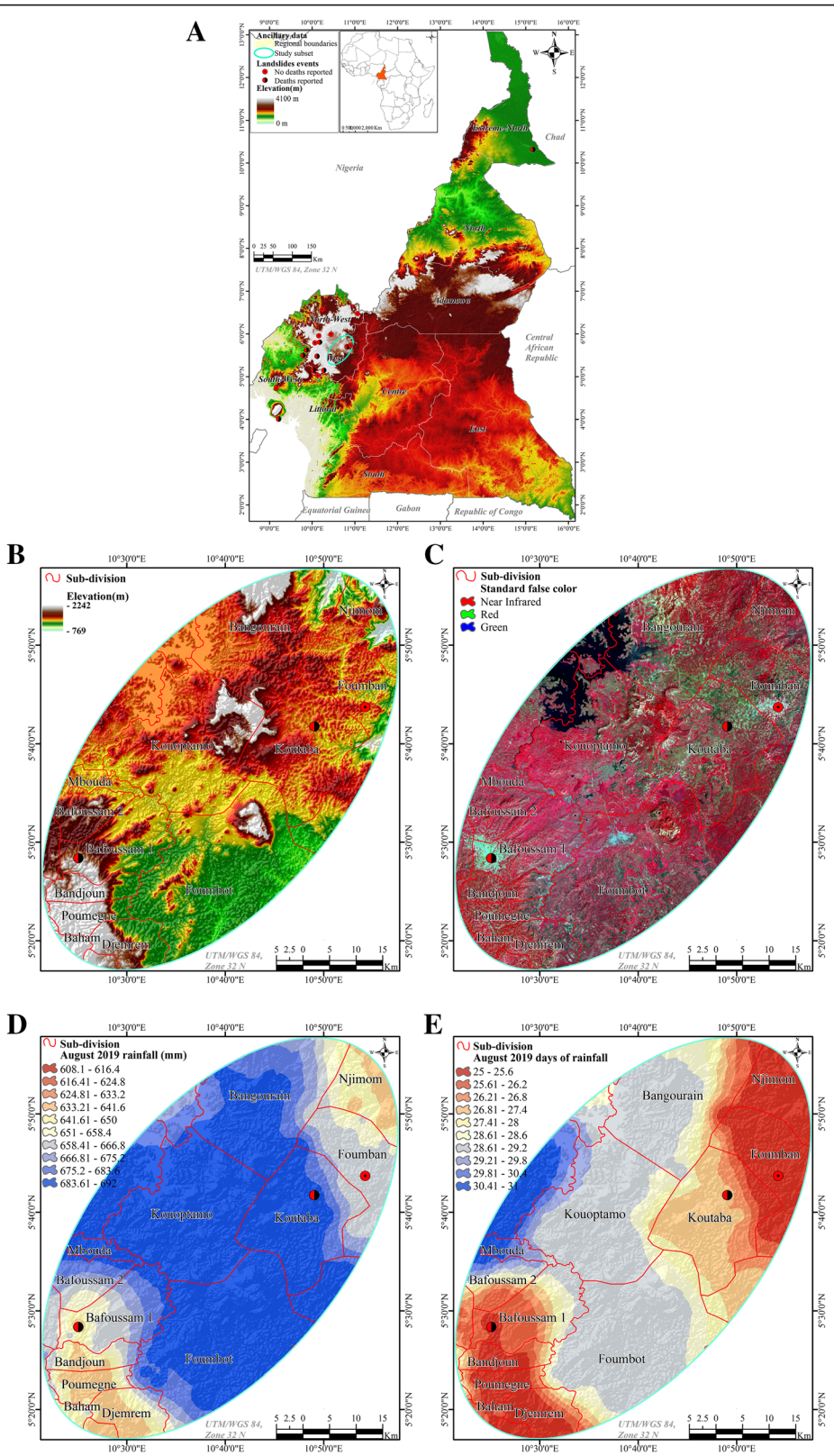

Fig. 1 The study location: **A** Landslides events on the elevation background in Cameroon, **B** & **C** Subsets of elevation and Landsat 8 satellite image. **D** Interpolation of average rainfall for August 2019, **E** Interpolation of days of rainfall for August 2019

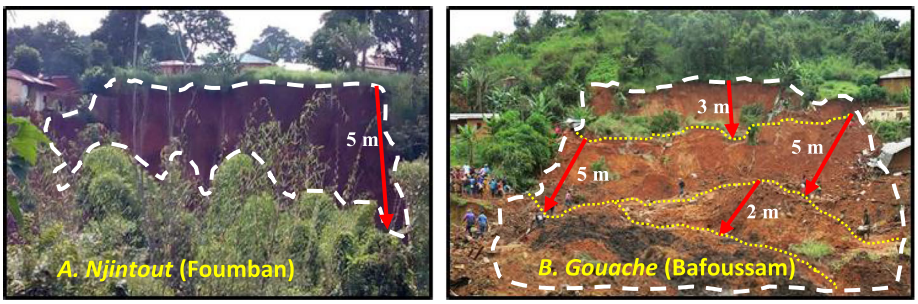

Fig. 2 Unscaled partial views of the scarps leaved by landslides of Foumban (in 2018) and Bafoussam (in 2019) – Both events were sudden with transitional to rotational movements, but the one in Foumban happened in one step, while the one in Bafoussam happened in three steps (yellow dashed), justifying three main blocks/stairs. Based on the soil horizontal surface, the sliding depths (arrows) are 5 m in Foumban, and 1 to 5 m in Bafoussam. The affected area was ≈30,100 m^2 in Foumban (IGMR-Penaye et al., 2018) and ≈ 15,051 m^2 in Bafoussam (IGMR-Kankeu & Ntchantcho, 2019)

by a landslide right after the event, based on fresh bare-earth exposure, and predict areas potentially exposed to upcoming events.

The spectral red band is computed for Landsat-8, band 4, and computed as a percentage between the 10 composed recent images before the landslide and the most recent post-event images. Areas with at least a *40%* increase in red reflectance are considered bare-earth, affected by the studied most recent landslide or exposed to landslide according to this criterion. To pursue, the soil moisture is assessed by adapting Normalized Multi-Band Drought Index, NMDI, of Wang and Qu (2007), to Landsat 8 spectroscopy. Basically, the NMDI monitors the soil and vegetation moisture using the following expression (1):

$$NMDI = \frac{R_{860nm} - (R_{1640nm} - R_{2130nm})}{R_{860nm} + (R_{1640nm} - R_{2130nm})} \quad (1)$$

where R_{860nm}, R_{1640nm} and R_{2130nm} represent the apparent at-sensor reflectance absorbed in the NIR and two SWIR wavelengths of the MODIS sensor measurements. However, the integration of the Landsat-8 band 6 that is closest to R_{1640nm}, gave poor results, and only bands 5 and 7 are used. The last step integrates a Digital Elevation Model's (DEM) slopes generating and thresholding. The slope values are extracted in degrees and their intervals are classified as follows: *gentle* (*0°–20°*), *fairly steep* (*20°–35°*), *steep* (*35°–45°*), *very steep* (*45°–60°*), and *extremely steep* (*60°–90°*). All the values ≥*20°* are considered to be landslide-triggering.

Further, noticing that a predominant triggering mechanism for landslides is rainfall (Petley et al. 2005), the Detecting Real-Time Increased Precipitation (DRIP) model leverage of NASA's Global Precipitation Measurement (GPM) was (re)built. It provides precipitation data with a more precise temporal window of occurrence for each potential event (Fayne et al., 2019). The DRIP algorithm identifies the likely timing of rainfall's peak, i.e., day and/or hour of the day, that has triggered the studied landslide event, and that matches the SLIP detected areas, every 16 days. Windows of 24, 48 and 72 h are tested to obtain continuous rainfall data and integrate into the model.

Data acquisition and preprocessing

This experiment was conducted in a desktop script environment of licensed software, Erdas Imagine 2020 version 16.6.0.1366, ArcGisPro version 2.5 and XLStats 2020.1.64570. Twelve Landsat 8 satellite images were downloaded from the United States Geological Survey website, and the landslide of the 28 October 2019 was fixed as origin. These were then distributed such as 11 before and one after the event (Appendix 1). Due to the important cloud cover in the rainy season, and its effect on interrupting the 16-days temporal resolution necessary for the processing, all the best images available were collected, several from the dry season, i.e., December to March, for at least two images per year. Basically, free Landsat images are all level-1 products, and delivered as digital numbers (DNs). The bands used here are 2 to 7, namely bands blue to SWIR2, with a spatial resolution of 30 m, and the panchromatic band (Band8) was used to rescale the spatial resolution to 15 m (Table 1).

Applying the Cosine Solar TAUZ (COST) radiometric calibration model of Chavez (1996) to the stacked image, blue-SWIR2, the digital numbers were converted from at-sensor radiance to top-of-atmosphere (TOA) reflectance via solar correction, and rescaled from 64-bit to unsigned 8-bit. Therefore, atmospheric corrections and haze reduction have helped to remove other noises and then approximate values of surface reflectance. The last step concerned the topographic correction that had addressed altitude artifacts. For the purpose of rainy season's land cover estimation, a classification map, change detection image and area expand function were applied (Appendix 2).

Table 1 Landsat OLI-TIRS bands characteristic

Spectral bands	Wavelengths Range (μm)	Spatial Resolution (m)
Band 1 - Ultra Blue	0.435–0.451	30
Band 2 - Blue	0.452–0.512	30
Band 3 - Green	0.533–0.590	30
Band 4 - Red	0.636–0.673	30
Band 5 - Near Infrared	0.851–0.879	30
Band 6 - Shortwave Infrared	1.566–1.651	30
Band 7 - Shortwave Infrared	2.107–2.294	30
Band 8 - Panchromatic	0.503–0.676	15
Band 9 - Cirrus	1.363–1.384	30
Band 10 - Thermal Infrared	10.60–11.19	100
Band 11 - Thermal Infrared	11.50–12.51	100

The other entry is the Shuttle Radar Topography Mission (SRTM) image of the area with a spatial resolution of 30 m. It was also downloaded from the USGS website and preprocessed by using the *void fill* method to create a Digital Elevation Model (DEM) and reduce the errors of commission in flat areas where landslides are unlikely, such as riverbeds, which may have similar red reflectance and moisture characteristics (Jiménez-Perálvarez et al. 2011; Fayne et al., 2019). Its integration into the model helps defining the slopes threshold for landslide triggering.

Another entry concerns the precipitation data. These data were combined from three main sources. The Tropical Rainfall Measuring Mission (TRMM) (Braun, 2011), Tropical Applications of Meteorology using Satellite data (TAMSAT) (Maidment et al., 2014) and some local meteorology services.

Adapted SLIP algorithm

The first step is defining the soil exposure, i.e., the percentage of non-vegetated land. Fayne et al. (2019) proposed it as a rate of change in the red band reflectance between the current image before the landslide and a composed image of the 10 red bands of the images before the landslide. The formula is expressed as follows (2):

$$\%\mathbf{Red_{change}} = \left(\frac{\mathbf{Red_{current}} - \mathbf{Red_{composite}}}{\mathbf{Red_{composite}}}\right) * \mathbf{100} \quad (2)$$

Where $\mathbf{Red_{current}}$ is the most recent Red band during or just after the landslide and is the 10 recent red bands just before the landslide. Then, the images should be collected for consecutives 16-days. In the present study, regarding the gap of almost 10 months in the same year between two Landsat 8 usable images, the percentage formula described above was leading to infinite values. Then the red difference was modified to an Inverse Normalized Difference Vegetation Index, INDVI, to assess the non-vegetated land. The INDVI is proposed as the spectral difference between the red and the NIR wavelength, such as (3):

$$\mathbf{INDVI} = \frac{\mathbf{Red} - \mathbf{NIR}}{\mathbf{Red} + \mathbf{NIR}} \quad (3)$$

After an average of the INDVI was computed for the 10 oldest images, referring to the landslide of the 28 October 2019 in Bafoussam. Then, the average INDVI was subtracted from December 2019 INDVI and the resulting image was normalized in percentage to obtain the fraction of non-vegetated land (4):

$$\mathbf{INDVIn} = \frac{\mathbf{INDVI} - \mathbf{INDVImin}}{\mathbf{INDVImax} - \mathbf{INDVImin}} * \mathbf{100} \quad (4)$$

Where INDVIn stands for the normalized INDVI image, min and max are the minimum and the maximum of the INDVI. Values starting at *40%* were selected as indicators for soil exposure to landslides as proposed by Fayne et al. (2019). A binned image was then created, with ***0*** for vegetated areas and ***1*** for non-vegetated areas, i.e., bare soil. Then, the vegetated class was expanded with factor ***2*** to approximate the land surface coverage in the rainy season, according to the classification statistics (Appendix 2).

Further, the soil moisture was assessed by using two indices. On one hand, the Modified Normalized Multi-Band Drought Index (MNMDI) (Fayne et al., 2019) was computed between the near infrared (NIR) and the shortwave infrared (SWIR2) bands (5):

$$\mathbf{MNMDI} = \frac{\mathbf{NIR} - \mathbf{SWIR2}}{\mathbf{NIR} + \mathbf{SWIR2}} \quad (5)$$

To confirm and complete the soil moisture information, the hydrothermal index composite was computed on the

other hand. This index is used to enhance soils, rocks and minerals, as well as vegetation cover at a regional scale, based on a multiple ratios approach computation between the visible and infrared wavelengths (Pour, 2014). The concerned band ratios are *SWIR1/SWIR (6/7)*, *Red/Blue (4/2)*, and *NIR/Red (5/4)*, while the result is a three principal components analysis image (Erdas Imagine, 2008). A linear regression was performed between each principal component and the MNMDI image, showing that the hydrothermal index PC3 was positively correlated to MNMDI with the highest determination coefficient (R^2) up to *82%* (appendix 3). The hydrothermal PC3 and the MNMDI stretching ranges are [*0–11*] and [*– 1.205–0.915*] respectively, their moisture thresholds were identified between [*1.5–11*] and [*0.08–0.915*] to create binned images. By adding up the two binned images, a new one was obtained, and then weighted ***0*** for no humidity and ***0.75*** for moisture.

As last step, the slope inclination value was computed based on the preprocessed DEM. In the Cameroon's landslides history and for the western highlands in specifically, the lowest slope for the hazard's occurrence was at Koutaba (in 2001; 2 deaths) on a slope of 22^0 (IGMR-Penaye et al., 2018; IGMR-Kankeu & Ntchantcho, 2019). For this reason, we choose the threshold ***20°***, proposed by Fayne et al. (2019) as significant to trigger landslide. After performing the *hillshade* processing to better highlight summits and valleys, the slope image was extracted in degrees. A binned image was coded, ***0*** for slopes less than ***20°***, and ***0.5*** for slopes at or above ***20°***. The three conditioned layers binned values are in Table 2.

The three layers were integrated using a simple weighted linear combination (SWLC) to map the areas where the conditions were met for sudden landslides. There are eight different values corresponding to the LHZ codes (Table 3). The SLIP process is described in Fig. 3 and the layers are represented in Fig. 4.

To validate the whole SLIP process, verification sites were chosen for each occurrence site, such as 2 in koutaba, 2 in Foumban and 5 in Bafoussam. The matching with affected sites defines accuracy.

Only remains the triggering factor identified as a long and huge rainfall. DRIP algorithm helps to model it.

Table 2 SLIP conditioned layers

	Conditions for LHZ	
	Excluded	*Included*
Bare soil	**0**	**1**
Soil moisture	**0**	**0.75**
Slope inclination	**0**	**0.5**

Table 3 LHZ codes and explanation

Codes	Conditions met
0	*None*
0.5	*Slope inclination*
0.75	*Soil moisture*
1	*Bare soil*
1.25	*Soil moisture & Slope inclination*
1.5	*Bare soil & Slope inclination*
1.75	*Bare soil & Soil moisture*
2.25	*Bare soil & Soil moisture & Slope inclination*

Adapted DRIP algorithm

The DRIP tool is adapted as the rainfall intensity and threshold corresponding to the SLIP landslide mapping. Monthly precipitations of the west-Cameroon were computed between 1948 and 2017 for Africa, completed for years 2018 and 2019 (Table 2). According to the Tropical Applications of Meteorology using Satellite and ground-based observations (TAMSAT) data, especially its TRMM Multi-satellite Precipitation Analysis (TMPA) datasets component and mapping models, daily rainfall for the Cameroons' west-highlands were between 6 mm and more than 10 mm between 1983 and 2012 (Maidment et al., 2014). The annual highest rainfall period is between the second decade of June and the first decade of October, with at least 15 mm to more than 25 mm per day (Maidment et al., 2014; Dezfuli et al., 2017). The rainfall data collected by the local agro-meteorology offices (October 2019) assess the rainfall of 28 to 29 October in Bafoussam up to 81 mm, in about 36 h, before the landslide. This represents *22%* of the 384 mm recorded for that month (Appendix 4). Ten groups of rainfall records were defined between June and October, that is 50 observations (Appendix 4). The month's selection is explained by the fact that all the landslides in Cameroon occurred in that 5 months interval, corresponding to the full rainy season (Table 4).

The rainfall increases from June to September with highest records in August, and decreases in October, before stopping in November. The trends are the same for the number of rainy days, although some local differences can be barely noticed between two zones. In addition, the rainfall zonation was done from the lower (zone 1) to the higher (zone10) records. Samples of zones ***1*** and ***8*** illustrate these two statements for 2019 (Fig. 5).

The general trend gives an average rainfall of 2615 mm for 1948–2018 and 2573 mm in 2019, representing respectively *79%* and *78%* of the 3300 mm maximum annual rainfall.

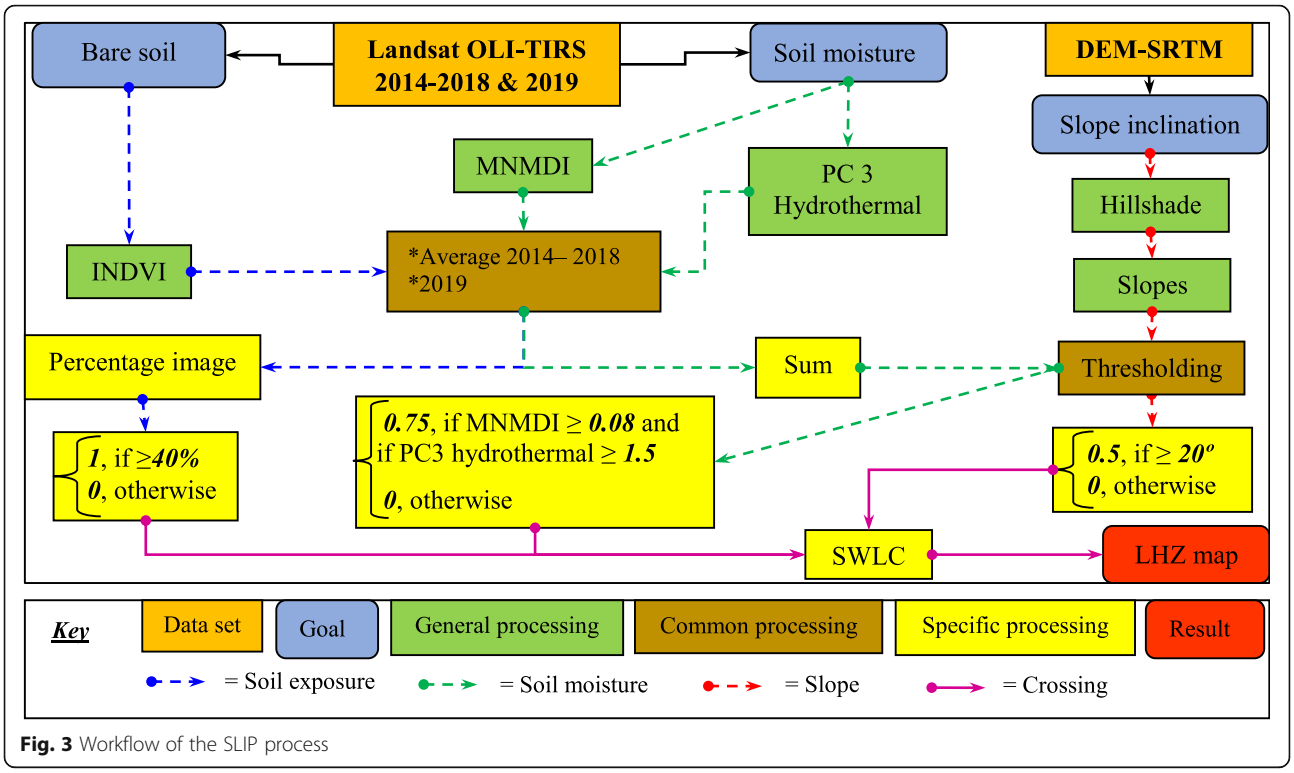

Fig. 3 Workflow of the SLIP process

August represents *25%* of the 5 months and October records about *14%* (Fig. 6). Moreover, the 81 mm of rainfall preceding the October 2019 landslide event represent *3.1%* of the 5 months and almost four times the total daily rainfall, as mapped by Maidment et al. (2014) and Dezfuli et al. (2017).

From the Table 4 above (including years 2012 to 2017), approximately ***53*** landslides have occurred in Cameroon between 1954 and 2019, and were all directly related to huge rainfall. As Fig. 7 illustrates, the highest month frequency corresponds to September with ***24*** occurrences (*45%*), followed by August with ***12*** occurrences (*22%*), October with ***11*** occurrences (*21%*), while June and July record the lowest same frequency of ***3*** occurrences (*6%*).

Further, their statistical distribution and variability were assessed by using the Weibull distribution. This method calculates a cumulative distribution function (CDF) or a probability density function (PDF) using the following eq. (6):

$$f(x) = \frac{\gamma}{\alpha}\left(\frac{x-\mu}{\alpha}\right)^{\gamma-1} \exp\left(-((x-\mu)/\alpha)^{\gamma}\right) \quad (6)$$

With $x \geq \mu$; $\gamma, \alpha > 0$

Where the parameters are γ the shape, μ the location and α the scale. Because the Weibull model studies strength and failure of a system in relation with time (Klein, 2009), this study assesses the stronger relationship to the failures between rainfall and days of rainfall for the period 1948–2018 average, and then for the year 2019, setting $=0.5$. The rainfall and days of rainfall data were rescaled by using the following ratios:

a) [***monthly rainfall ÷ monthly total of rainy days***]
b) [***monthly rainy days ÷ monthly total days***]

The probabilities of failure and success were defined for both sets of data such as (7, 8):

$$\mathbf{PF}(x) = \frac{n_x}{N+1} \quad (7)$$

$$\mathbf{PS}(x) = 1 - PF \quad (8)$$

With *PF* and *PS* representing the probability of strength to failure and the probability of success. Then, their probabilities of strength to failure are suitable to be used as the *z* value in the standard PDF computation, which is defined as a normal distribution. Purposely and based on the data, the averages (≈*3* and ≈*4*) and the standard deviations (≈*1*) of the mean daily rainfall and days of rainfall were computed for the two periods, and the PDF curves were superimposed on each other to find intersections (Fig. 8a & b).

From the intersection of the two PDF curves, a set of thresholds were defined in a conditioning algorithm, with six explanatory variables (X), i.e., before landslide (1948–2018) and one dependent variable (Y), i.e., after landslide (2019). The whole conditioning algorithm is written in eq. 9 (***i-vii***) as follows:

$$X_{1.1.} = \begin{cases} \mathbf{1}\ if\ \boldsymbol{PDF}_{\mathbf{1948-2018}}\ rainfall\ frequency \leq \mathbf{0.229} \\ \mathbf{0}\ Otherwise \end{cases}$$

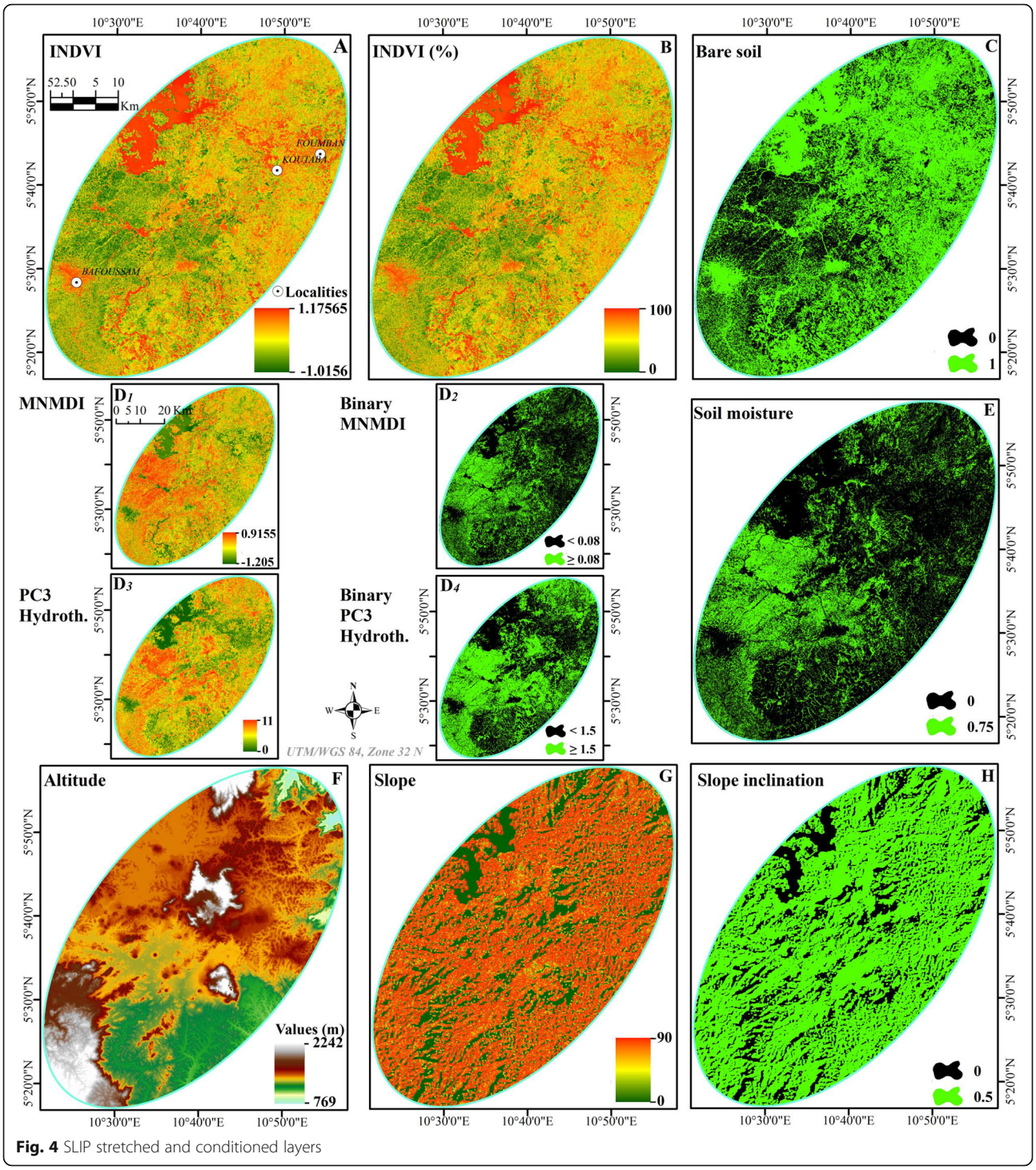

Fig. 4 SLIP stretched and conditioned layers

$$X_{1.2.} = \begin{cases} \mathbf{1}\ if\ \mathbf{0.228} > \boldsymbol{PDF}_{\mathbf{1948-2018}}\ rainfall\ frequency \leq \mathbf{0.394} \\ \mathbf{0}\ Otherwise \end{cases}$$

$$X_{1.3.} = \begin{cases} \mathbf{1}\ if\ \mathbf{0.394} > \boldsymbol{PDF}_{\mathbf{1948-2018}}\ rainfall\ frequency \\ \mathbf{0}\ Otherwise \end{cases}$$

$$X_{2.1.} = \begin{cases} \mathbf{1}\ if\ \boldsymbol{PDF}_{\mathbf{1948-2018}}\ days\ of\ rainfall\ frequency \leq \mathbf{0.229} \\ \mathbf{0}\ Otherwise \end{cases}$$

$$X_{2.2.} = \begin{cases} \mathbf{1}\ if\ \mathbf{0.229} > \boldsymbol{PDF}_{\mathbf{1948-2018}}\ days\ of\ rainfall\ frequency \leq \mathbf{0.394} \\ \mathbf{0}\ Otherwise \end{cases}$$

$$X_{2.3.} = \begin{cases} \mathbf{1}\ if\ \mathbf{0.394} > \boldsymbol{PDF}_{\mathbf{1948-2018}}\ days\ of\ rainfall\ frequency \\ \mathbf{0}\ Otherwise \end{cases}$$

Table 4 Landslide causes and consequences in Cameroon to the best of recording

Month/Year	Location	Causes	Main casualties and losses
September 1954	Nchingang, Lebialem	Slopes' agriculture, woodcutting and huge rainfall	Bridges destroyed followed by flooding
September 1956	Beine, Lebialem	Slopes' agriculture and huge rainfall	3 deaths; houses and bridges destroyed followed by flooding; farms flooded and destroyed
September 1957	Fomenji, Lebialem	Huge rainfall	12 deaths, bridges and farms destroyed
August 1973	Fonengé, Lebialem	Huge rainfall	1 death; dozens of houses destroyed; 300 homeless
August 1978	Fossong-Wetcheng (Dshang)	Huge rainfall	6 deaths; farms destroyed
June 1988	Bamboko, Melong mt Manengouba	Huge rainfall	8 deaths; bridges and houses destroyed
June 1991	Pinyin	Thundershowers	Plantations destroyed
July 1991	Limbe, Mt Cameroun	Public works on slopes; Huge rainfall	1 death; 1 house destroyed
September 1991	Pinyin, Santa, Bamenda	Slopes' agriculture and huge rainfall	12 deaths; 2 houses destroyed
12 September 1992	Santa, Bamenda	Slopes' agriculture and huge rainfall	12 deaths; 5 houses destroyed
September 1992	Fomenji, Abi, Fonengé	Slopes' agriculture and huge rainfall	12 deaths; houses, bridges and farms destroyed
September 1993	Bafaka	Huge rainfall	Farms and houses destroyed
September 1994	Fomenji, fotang, Fonengé	Slopes' agriculture and huge rainfall	6 bridges and 10 houses destroyed
September 1995	Bafaka, Ndian, Mt Rumpi	Earthquakes (intensity VII on Richter scale) and rainfall	3 deaths; 1 house, farms and forests destroyed.
September 1997	Sho, Belo	Huge rainfall; perched water source; slopes' agriculture; woodcutting	2 deaths; 1 house, 1 road destroyed followed by several weeks of traffic interruption; farms destroyed.
September 1997	Gouata, Dschang (Mt Bamboutos)	Huge rainfall	1 death and farms destroyed
September 1997	Batié	Sand digging and huge rainfall	Farms destroyed
July 1998	Bingo, Belo	Huge rainfall	5 deaths and 3 houses destroyed
August 1998	Bamumba, wabane Lebialem	Slight earth shaking and rainfall	5 injured; 11 houses destroyed; bridges and farms destroyed.
August 1998	Abi, Ako, Atsuela, Babong	Rainfall	1 injured; houses and farms destroyed
September 1998	Anjin, Belo	Slopes' agriculture, woodcutting and huge rainfall	2 deaths; 1 house and farms destroyed;
September 2000	Rom Nwah	Earthquakes (intensity IV on Richter scale) and rainfall	6 deaths; 17 injured; 7 houses destroyed;
June 2001	Limbé	Earthquakes (intensity IV on Richter scale) and rainfall	24 deaths, 2800 homeless, 120 houses destroyed
10 September 2002	Bana-Bafang	Slopes' agriculture and huge rainfall	10 deaths; houses destroyed
20 July2003	Magha'a and Atsuela	Slopes' agriculture, breeding, woodcutting and huge rainfall	22 deaths; 50 deaths cattle; houses; roads and farms destroyed.
August 2003	Bafou	Rainfall	2 deaths; 1 house destroyed
August 2003	Wabane	Huge rainfall and flooding	1 death
27 September 2007	Abuh	Rainfall	Plantations destroyed
September 2008	Fondonera	Huge rainfall	Farms destroyed
October 2008	Moumé-Bafang	Huge rainfall	1 death; 103 homeless; 12 houses and 1 road destroyed;
October 2009	Bamenda-Akum	Huge rainfall causing collapse and blocks subsidence	Main road destroyed with several days of traffic interruption

Table 4 Landslide causes and consequences in Cameroon to the best of recording *(Continued)*

Month/Year	Location	Causes	Main casualties and losses
October 2010	Bamenda	Huge rainfall causing collapse and blocks subsidence	7 deaths; 7 houses destroyed; 50 homeless;
23 October 2011	Koutaba	Bare slopes and huge rainfall	2 deaths;
August, September and October of every year including 2012 to 2017	Mbo and Ndop plains	Huge rainfall, slopes' agriculture and breeding	Farms and roads destructions
4 & 5 September 2018	Foumban	Huge rainfall causing collapse and blocks subsidence	Houses and roads destroyed
28 & 29 October 2019	Bafoussam	Slopes' agriculture, breeding, woodcutting and huge rainfall	45 deaths; 300 homeless; dozens of houses destroyed

(Sources – Ayonghe et al., 2002; Tchindjang, 2013; IGMR-Penaye et al., 2018; IGMR-Kankeu & Ntchantcho, 2019)

$$Y = \begin{cases} \mathbf{1}\ if\ \boldsymbol{PDF_{2019}} \le \mathbf{0.29} \\ \mathbf{0}\ Otherwise \end{cases}$$

Then the probability of rainfall-triggered landslide is calculated by performing the logistic function. This is a classification algorithm useful for predicting binary outcome (*1/0, Yes/No, True/False*) given a set of predictor variables. It allows computing a multivariate regression between a binary dependent variable and several independent variables (Atkinson and Massari, 1998). Multiple logistic regression assumes that observations are independent and the natural log of the odds ratio and the measurement variables have a linear relationship. The quantitative relationship between the occurrence and its dependency on several variables can be expressed in the form of a logit function (10):

$$\boldsymbol{P_{(Ev.=1)}} = \frac{\boldsymbol{e^{Z_{Ev.}}}}{\mathbf{1}+\boldsymbol{e^{Z_{Ev.}}}} \quad (10)$$

Where $\boldsymbol{P_{Ev}}$, is the probability of an event occurring. In this case, the event is the daily rainfall threshold to trigger the landslide, and then being equal to $\boldsymbol{1}$ in the interval $(0, 1)$. $\boldsymbol{Z_{Ev.}}$ is the linear relationship of the event's occurrence with independent variables, and it is expressed as (11):

$$\mathbf{Z_{Ev.}} = \mathbf{b_0} + \mathbf{b_1 x_1} + \mathbf{b_2 x_2} + \ldots \mathbf{b_n x_n} \quad (11)$$

Where $\boldsymbol{b_0}$ is the intercept of the model, the $\boldsymbol{b_i}$ ($\boldsymbol{i = 0, 1, 2, \ldots, n}$) are the slope coefficients of the logistic regression model, and the $\boldsymbol{x_i}$ ($\boldsymbol{i = 0, 1, 2, \ldots, n}$) are the explanatory variables. Figure 9 synthesizes the processing.

The validation of DRIP model was conducted through a double accuracy assessment. The first is the confusion matrix, extracted from the logistic regression's classification table, based on the true positive rate, *TPR*, defining the ratio of all positive cases correctly predicted, and the false positive rate, *FPR*, expressing the ratio of all negative cases that are incorrectly predicted to be positive, under a defined threshold value. They are formulated as (12 & 13):

i) $\mathbf{TPR} = \mathbf{TP}/(\mathbf{TP}+\mathbf{FN})$ (12)

ii) $\mathbf{FPR} = \mathbf{FP}/(\mathbf{FP}+\mathbf{TN})$ (13)

The second is the positive predictive value, PPV, and the negative predictive value, NPV, that are respectively

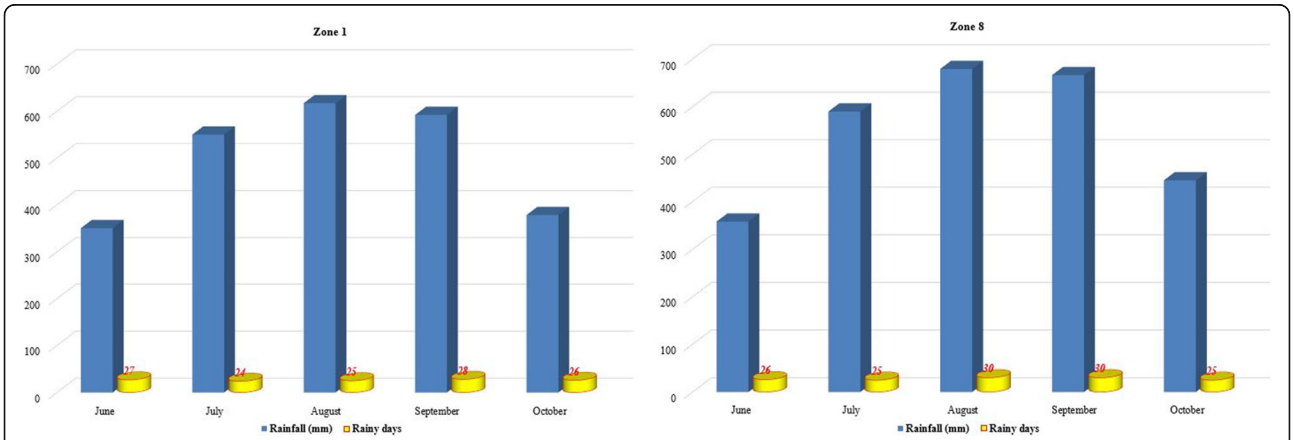

Fig. 5 Monthly rainfall and rainy days sampled for two zones of the study area in 2019 (Source – Local agro-meteorology offices compilation)

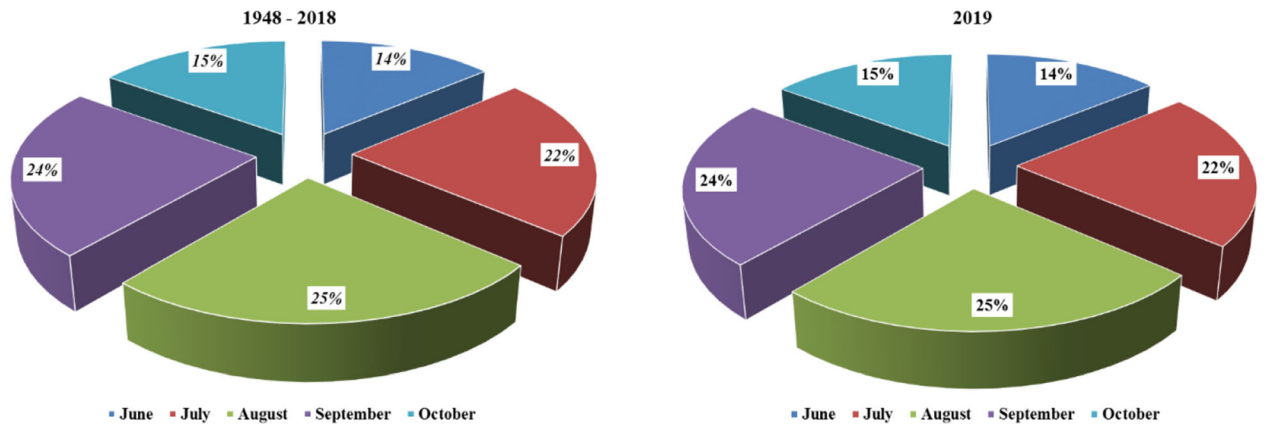

Fig. 6 Percentage of monthly rainfall between June and October

the proportions of positive and negative results were computed. They are expressed as follows (14 & 15):

$$\text{i)}\quad \mathbf{PPV}=\mathbf{NTP}/(\mathbf{NTP}+\mathbf{NTN}) \tag{14}$$

$$\text{ii)}\quad \mathbf{NPV}=\mathbf{NFP}/(\mathbf{NFP}+\mathbf{NFN}) \tag{15}$$

Modelling rainfall-triggered landslides from the survival analysis perspective

The method of Caine (1980) was used to model the relation of rainfall to landslides. This process suggests a general threshold that works for time paces between 10 min and 10 days, using the rainfall intensity (***I, mm/hr***) and duration (***D, hr***). Here, the quantity of monthly rainfall was expressed as a function of the duration (***Q, mm/hr***) in the following eq. (16):

$$I=\frac{Q}{D}=\alpha D^{\beta}\Leftrightarrow Q=\alpha D^{\beta} \tag{16}$$

The values of α and β are defined by using the Cobb-Douglas regression model in the formulation (17):

$$\log(Q)=\log(\alpha)+\beta*\log(D) \tag{17}$$

The second step consists in assessing the spatial variability of the phenomenon. A spatial autoregressive model (SAR) enables to decompose the spatial process for a known site s, based on a random variable $Z_{(s)}$, as follows (18):

$$\begin{aligned} &Z_{(s)}=\mu_{(s)}+\varepsilon_{(s)}\\ &\mu_{(s)}=\left[Q_{(s)};LHZ_{(s)}\right]\\ &LHS_{(s)}=aQ^{b}(s)\Leftrightarrow\mu_{(s)}=aQ^{b}(s) \end{aligned} \tag{18}$$

Where a and b are similarly extracted as for α and β. Therefore (19):

$$Z_{(s)}=LHZ_{(s)}+\varepsilon_{(s)}=\alpha aD^{\beta b}+\varepsilon_{(s)} \tag{19}$$

Where, $\mu(.)$ is the spatial characterization and $\varepsilon(s)$ is a centered random variable or error, α and a result from computing exponential of the intercept, and $LHZ_{(s)}$ integrates the four binary codes corresponding to at least

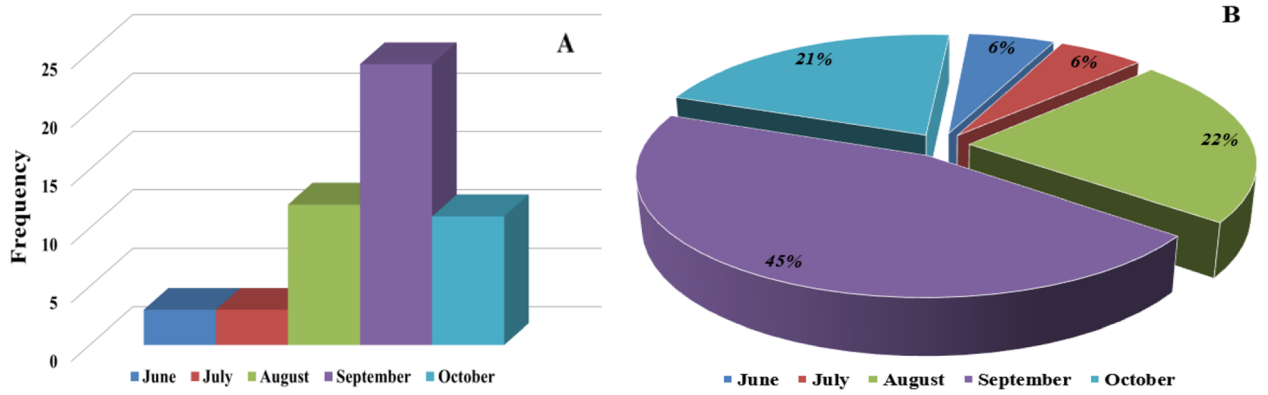

Fig. 7 Monthly frequency (**A**) and percentage (**B**) of landslides between 1954 and 2019

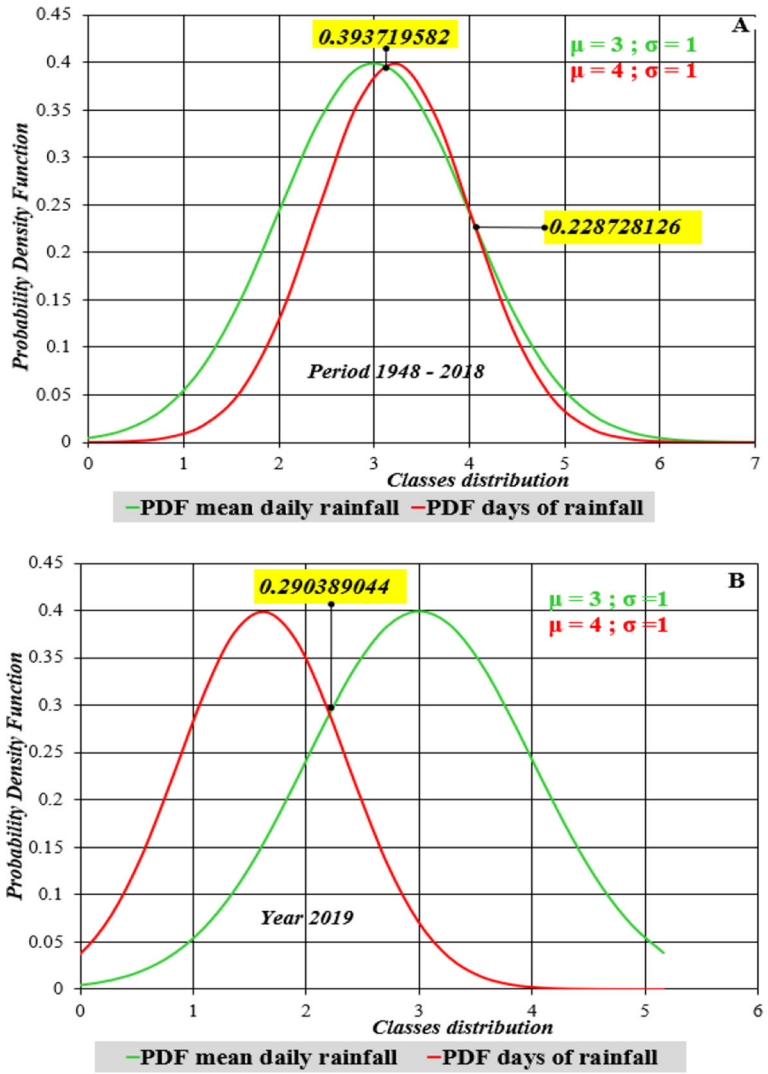

Fig. 8 Individual PDF curves and their intersections before (**A**) and in (**B**) 2019

two conditions met (Table 3) plus the fifth spatially closest code.

For an unknown site, S_0, a prediction $\hat{z}_{s_0}$ of Z_{s_0} is interpolated using the observations Z_{s_1}, Z_{s_1},... Z_{s_n} through the kriging process, expressed such as (20):

$$\hat{z}_{s_0} = \lambda_1 Z_{s_1} + \lambda_2 Z_{s_2} + \ldots + \lambda_n Z_{s_n} \tag{20}$$

Then follows the Cox proportional hazards model. Originally, this model is used on the medical field to assess the probability that an individual will experience an event (for example, death) within a small-time interval, given that the individual has survived up to the beginning of the interval (Cox, 1972). The methodology mostly looks at the probability that given hazards, as the opposite phenomenon of hazards, may occur for a given actual occurrence. Although these models were not originally oriented spatial, they have been progressively integrated in geospatial analysis. Recent applications concerned fire hazard probabilities (Cyr et al., 2007) and factors of a space colonization (Baudains et al., 2015).

Theoretically, the hazard function for this case study is expressed such as (21):

$$\begin{aligned} \lambda(t \mid Z_{s_i}) &= \lambda_0(t)\ \exp(\beta_1 Z_{s_1} + \beta_2 Z_{s_2} + \ldots + \beta_n Z_{s_n}) \\ &= \lambda_0(t)\ \exp\left(\beta * \overline{Z}_{s_1 - s_n}\right) \end{aligned} \tag{21}$$

It gives the hazard function at time t for any unknown site S_0 with covariate vector that are the known sites of occurrence Z_s. There are five known sites that are, one (*1*) in Koutaba, three in Foumban (*3*) and one in Bafoussam (*1*). There are also nine verification or unknown sites, distributed such as two in Koutaba, two in Bafoussam and

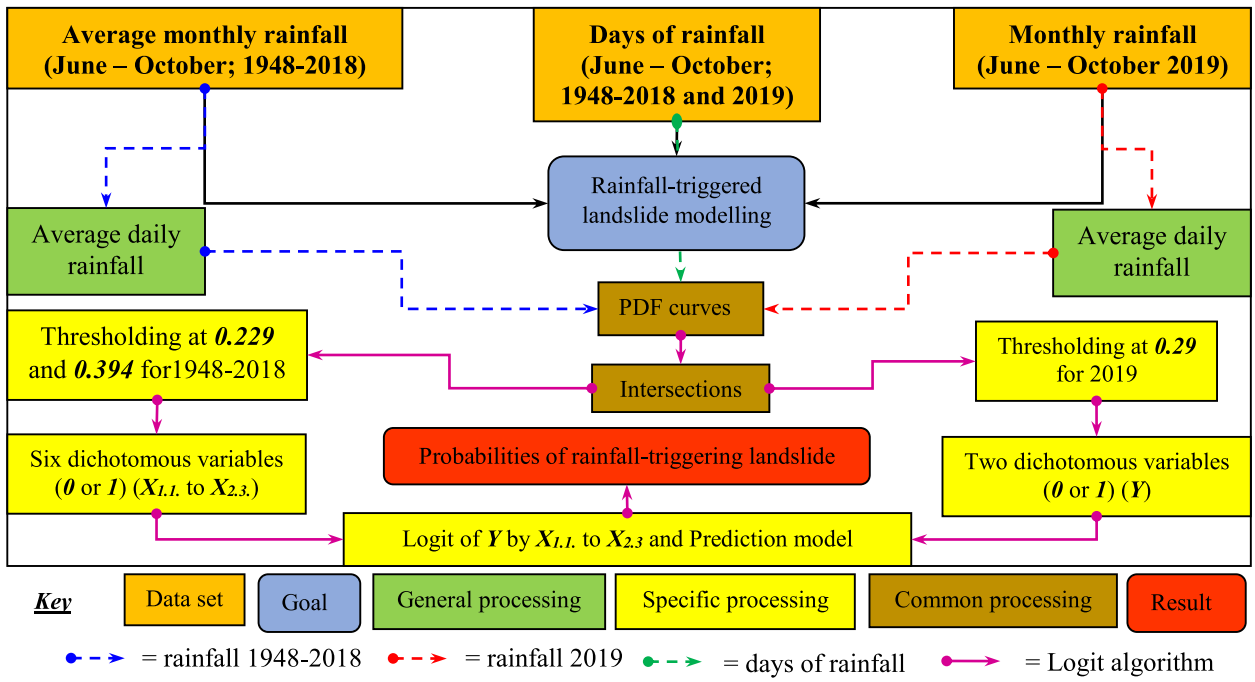

Fig. 9 Workflow of the DRIP process

five in Bafoussam. The model is built for the entire period, 1948–2019.

Results and discussions

Landslide Hazard zonation (LHZ) SLIP-based map

The SLIP outcome is a map identifying the landslide zones of occurrence in eight classes (Fig. 10). The lowest class value, ***0***, stands for none condition met and the highest-class value, ***2.25***, corresponds to the landslide full conditions. The study subset is widely exposed to landslides hazard at different degrees. The visual patterns appraisal was conducted by zooming on the three localities of Koutaba, Foumban and Bafoussam, subject to landslides in October, 2011, September 2018 and October 2019. Generally, at least two conditions are met for the occurrence of the event and the dominant trend is the combination *bare soil & slope inclination* (***1.5***) conditions.

i) In Koutaba, the occurrence site matches classes coded ***1.5*** (*Bare soil & Slope inclination*), ***1.75*** (*Bare soil & Soil moisture*) and ***2.25*** (*Bare soil & Soil moisture & Slope inclination*). Its two sites of observations are extended between classes ***0*** and ***1.5***.
ii) In Foumban, the landslide sites mostly met two conditions and are surrounded by the three conditions, that is from the class coded ***1.25*** (*Soil moisture & Slope inclination*) to the class coded ***2.25*** (*Bare soil & Soil moisture & Slope inclination*). Its two verification sites fall between classes ***0*** and ***2.25***, but are not concerned with the class coded ***1.75***.
iii) In Bafoussam, the landslide site of Gouache matches the class coded ***1.5*** (*Bare soil & Slope inclination*) and is bounded by classes coded ***1.25*** (*Soil moisture & Slope inclination*) and ***1.75*** (*Bare soil & Soil moisture*). Among its five verification sites, four (2, 3, 4 & 5) are extended between the classes coded ***1.5*** and ***2.25***, while the remaining site (1) matches the class coded ***1*** (Bare soil), surrounded by classes coded ***1.75*** and ***2.25***.

Statistically, the area where at least two conditions were met represents *67.5%* of the study area. The largest area is occupied by the class coded ***1.5*** (*Bare soil & Slope inclination*) with 1709.47 km^2 that represents *44%* of the research area. Then follow the classes coded ***1.25*** (*Soil moisture & Slope inclination*; 629.92 km^2; *16%*), ***2.25*** (*Bare soil & Soil moisture & Slope inclination*; 217.75 km^2; *6%*) and ***1.75*** (*Bare soil & Soil moisture*; 69.34 km^2; *2%*). The none condition class, ***0***, as well as the single conditions classes coded ***0.5*** (*Slope inclination*), ***0.75*** (*Soil moisture*) and ***1*** (*Bare soil*), cover 1276.29 km^2, representing *32.5%* of the study subset (Fig. 11).

Triggering rainfall DRIP-based thresholds

The highest concentration of rainfall and days of rainfall reveals information related to landslides occurrence (Fig. 12).

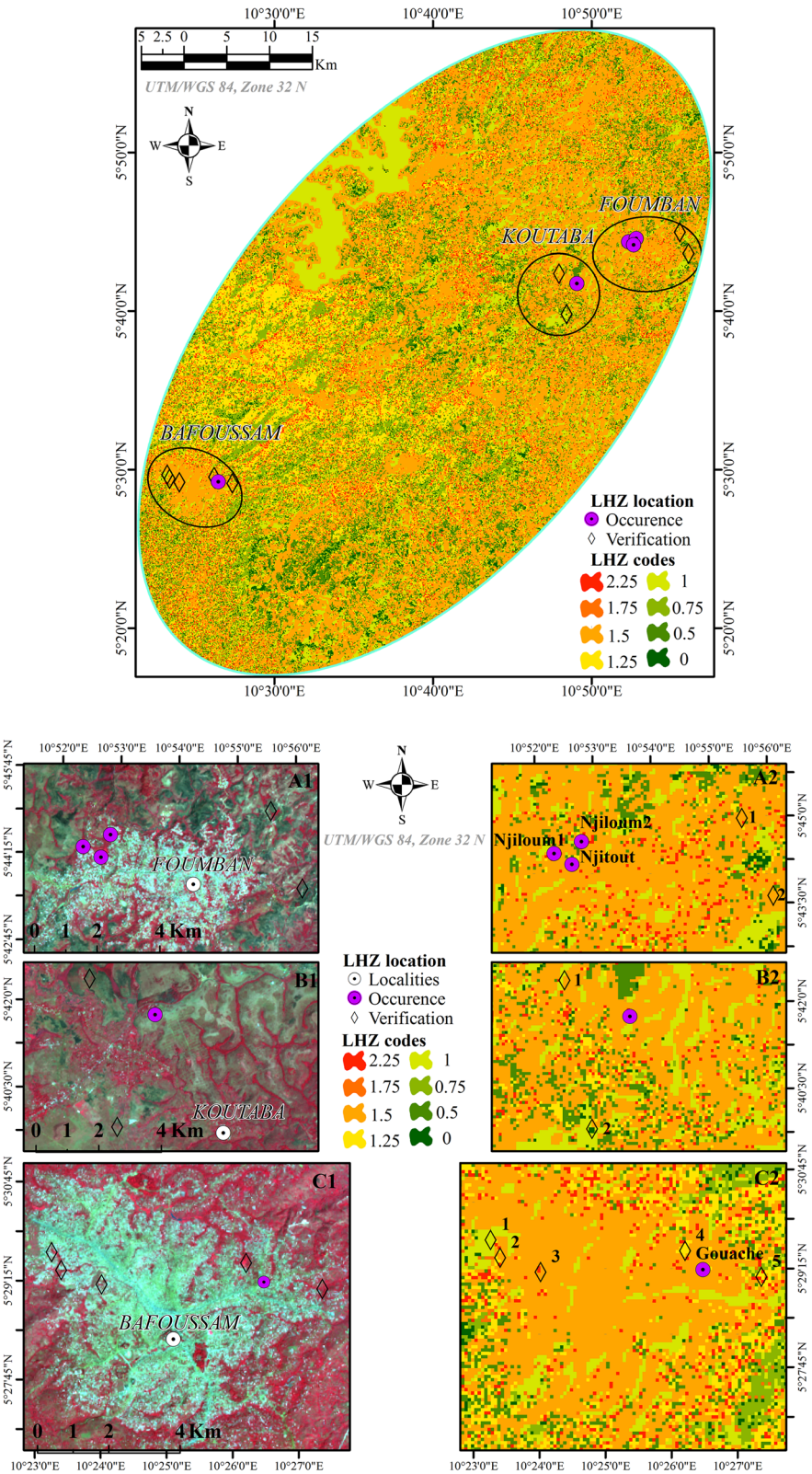

Fig. 10 LHZ mapping: **A** The eight classes of landslide occurrence extent and corresponding codes, **B1** & **B2** Patterns and sites location in Foumban, **C1** & **C2** Patterns and sites location in Koutaba, **D1** & **D2** Patterns and sites location in Bafoussam

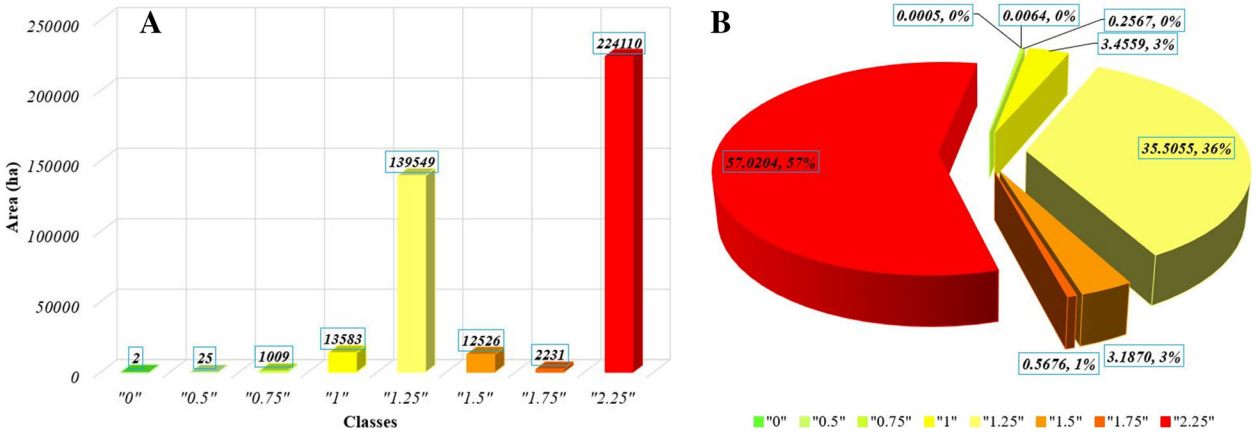

Fig. 11 Areas (**A**) and percentages (**B**) of LHZ per classes

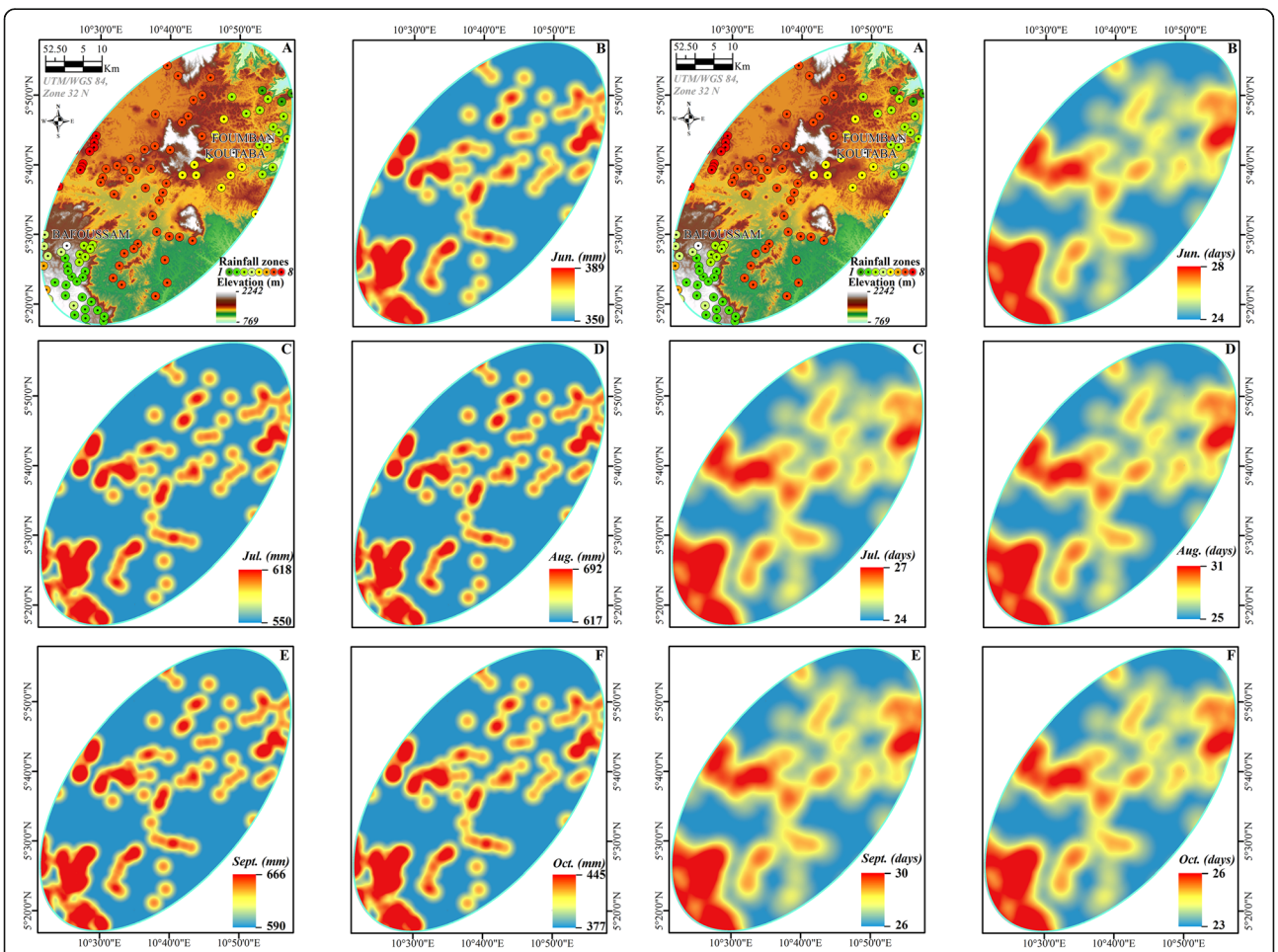

Fig. 12 Spatial distribution of daily rainfall (**left**) and days of rainfall (**right**) from June to October

Table 5 Different probabilities expressed by the prediction model

Probability Ranges	$f(Y) \leq 0.29$ Expression	Landslide occurrence
$f_{(x_1)}; f_{(x_2)} \leq 0.229$	$Exp(-(-17.34 + 20.31))/1 + exp(-(-17.34 + 20.31))$	**4.88%**
$0.229 < f_{(x_1)}, f_{(x_2)} \leq 0.394$	$Exp(-(-17.34 - 0.0000000013 + 0.0000000002))/(1 + exp(-(-17.34 - 0.0000000013 + 0.0000000002)))$	**99.99%**
$f_{(x_1)}, f_{(x_2)} \geq 0.394$	$Exp(-(-17.34 + 0.0000000003 - 0.000000002))/(1 + exp(-(-17.34 + 0.0000000003 - 0.000000002)))$	**99.99%**
$f_{(x_1)} \leq 0.229$, $0.229 < f_{(x_2)} \leq 0.394$	$Exp(-(-17.34 + 20.31 + 0.0000000002))/(1 + exp(-(-17.34 + 20.31 + 0.0000000002)))$	**4.88%**
$f_{(x_1)} \leq 0.229$, $f_{(x_2)} > 0.394$	$Exp(-(-17.34 + 20.31 - 0.000000002))/(1 + exp(-(-17.34 + 20.31 - 0.000000002)))$	**4.88%**
$0.229 < f_{(x_1)} \leq 0.394$, $f_{(x_2)} \leq 0.229$	$Exp(-(-17.34 + 0.0000000013))/(1 + + exp(-(-17.34 + 0.0000000013)))$	**99.99%**
$f_{(x_2)} \leq 0.229$, $f_{(x_1)} > 0.394$	$Exp(-(-17.338 + 0.0000000002))/(1 + exp(-(-17.338 + 0.0000000002)))$	**99.99%**
$0.229 < f_{(x_1)} \leq 0.394$, $f_{(x_2)} > 0.394$	$Exp(-(-17.34 - 0.0000000013 + 0.000000002))/(1 + exp(-(-17.34 - 0.0000000013 + 0.000000002)))$	**99.99%**
$0.229 < f_{(x_2)} \leq 0.394$, $f_{(x_1)} > 0.394$	$Exp(-(-17.34 + 0.0000000002 + 0.00000000035))/(1 + exp(-(-17.34 + 0.0000000002 + 0.00000000035)))$	**99.99%**

The maps outputted from the rainfall data show how the three sites, Koutaba, Foumban and Bafoussam match the main rainfall hot spots. The largest and densified spot is in the southern area, the second one is in the west and the third one is in the northeast area. At first sight and according to a visual comparison with the SLIP algorithm output, it may be assumed that rainfall concentration, in terms of quantity and number of days, is related to landslides.

The further analysis of the logistic regression helps to comfort and discuss this assumption. The prediction model of rainfall-triggered landslide thresholds is expressed as (22):

$$\begin{aligned} \mathbf{f}(Y) = \boldsymbol{Exp}(&-(-\mathbf{17.338} + \mathbf{20.31}*X_{1.1.} - \mathbf{0.0000000013}*X_{1.2.} \\ &+ \mathbf{0.0000000003}*X_{1.3.} + \mathbf{0.0000000002} - \mathbf{10}*X_{2.2.} \\ &- \mathbf{0.000000002}*X_{2.3.})) \div (\mathbf{1} + \boldsymbol{Exp}(-(-\mathbf{17.338} \\ &+ \mathbf{20.31}*X_{1.1.} - \mathbf{0.0000000013}*X_{1.2.} + \mathbf{0.0000000003}*X_{1.3.} \\ &+ \mathbf{0.0000000002} - \mathbf{10}*X_{2.2.} - \mathbf{0.000000002}*X_{2.3.}))) \end{aligned} \quad (22)$$

As a reminder, X_1 represents the rainfall frequency and X_2 stands for the days of rainfall frequency between

Table 6 Equations of ANOVA regression for the observed sites

Observed sites (Period)	Model	Values
S1-Njiloum1 (1948–2018)	$\mathbf{0.03004} * \mathbf{18119.1} * \mathbf{607}^{\mathbf{2.012}*(\mathbf{-0.488})}$	1.0073
S2-Njiloum2 (1948–2018)	$\mathbf{0.03004} * \mathbf{33858} * \mathbf{607}^{\mathbf{2.012}*(\mathbf{-0.2612})}$	35.0509529712193
S3-Njitout (1948–2018)	$\mathbf{0.03004} * \mathbf{158816.73} * \mathbf{607}^{\mathbf{2.012}*(\mathbf{-0.394})}$	29.6676110831837
S4-Koutaba (1948–2018)	$\mathbf{0.0305} * \mathbf{1812} * \mathbf{610}^{\mathbf{1.694}*(\mathbf{-0.493})}$	0.260802712270763
S5-Bafoussam (1948–2018)	$\mathbf{0.0233} * \mathbf{13589.52} * \mathbf{613}^{\mathbf{1.76}*(\mathbf{-0.3463})}$	6.33339140678556
Mean 1948–2018		**14.4640116346919**
S1-Njiloum1 (2019)	$\mathbf{18255.1} * \mathbf{55603585} * \mathbf{614}^{\mathbf{1.1724}*(\mathbf{-0.886})}$	1,878,436,394.94023
S2-Njiloum2 (2019)	$\mathbf{18255.1} * \mathbf{58869398061659300} * \mathbf{614}^{\mathbf{1.1724}*(\mathbf{-1.473})}$	16,453,557,989,053,200
S3-Njitout (2019)	$\mathbf{18255.04} * \mathbf{309547810768.523} * \mathbf{614}^{\mathbf{1.1724}*(\mathbf{-1.13})}$	1,143,698,653,144.39
S4- Koutaba (2019)	$\mathbf{18255.04} * \mathbf{55603585} * \mathbf{616}^{\mathbf{1.63}*(\mathbf{-0.903})}$	79,529,751.9255277
S5-Bafoussam (2019)	$\mathbf{13691.28} * \mathbf{41702688.98} * \mathbf{618}^{\mathbf{1.94}*(\mathbf{-0.646})}$	181,480,394.584158
Mean 2019		**3,290,940,765,430,580**

Table 7 Normalized and incremented/decremented coefficients

Years	Coefficient status	Observed sites				
		S1-Njiloum1	*S2-Njiloum2*	*S3-Njitout*	*S4-Koutaba*	*S5-Bafoussam*
1948–2018	**Normalized**	**0.0696**	**2.423**	**2.051**	**0.01803**	**0.4378**
	Incremented / Decremented at a pace of 0.25	0.319	2.173	1.801	0.26803	0.6878
		0.569	1.923	1.551	0.51803	0.9378
		0.819	1.673	1.301	0.76803	1.1878
		1.696	1.423	1.051	1.01803	1.4378
2019	**Normalized**	**0.00000057**	**4.999**	**0.000347**	**0.000000024**	**0.00000006**
	Incremented / Decremented at a pace of 0.25	0.25000057	4.749	0.250347	0.250000024	0.25000006
		0.50000057	4.499	0.500347	0.500000024	0.50000006
		0.75000057	4.249	0.750347	0.750000024	0.75000006
		1.00000057	3.999	1.000347	1.000000024	1.00000006
μ of normalized values		**0.0348**	**3.7114**	**1.0257**	**0.009**	**0.2189**

1948 and 2018, while Y is their intersection for the year 2019 (Table 5).

There are six ranges of probability over nine (6/9) that are rainfall-triggered landslides event, Y. The landslide probability is obvious at *99.99%* when $\mathbf{0.229 \le X_1}$, $\mathbf{X_2 < 0.394}$ or $\mathbf{X_1, X_2 \ge 0.394}$. However, the influence of the rainfall frequency on the landslide is higher than the days of rainfall frequency, such as for $\mathbf{X_1 \ge 0.229}$ and $\mathbf{X_1 \ge 0.394}$, the probability remains *99.99%*, no matter if the rainfall frequency $\mathbf{X_2 < 0.229}$. Reversely, for all rainfall frequency $\mathbf{X_1 \le 0.229}$, the probability of landslide occurrence is very low, *4.88%*, no matter if for the days of rainfall frequency, $\mathbf{0.229 < X_2 \le 0.394}$ or $\mathbf{X_2 \ge 0.394}$. Consequently, the frequency of rainfall alone is able to trigger a landslide event in the study area once the minimum threshold of ***0.229*** is reached. Therefore, the adapted DRIP approach shows suitability to distinguish landslide and no-landslide for one common frequency.

Table 8 LHZ codes matching and surrounding the verification sites

Sites	Corresponding LHZ codes	S_0 selected codes
Koutaba-Verification 1	**0.01*; 0.5; 0.75; 1; 1.5**	**0.01[a]; 0.01; 0.5; 0.5; 0.75; 0.75; 1; 1; 1.25; 1.5**
Koutaba-Verification 2	**0.01; 0.5; 0.75; 1; 1.25**	
Foumban-Verification 1	**0.01; 0.75; 1; 1.25; 1.5**	**0.01; 0.5; 0.75; 0.75; 1; 1; 1.25; 1.5; 1.5; 2.25**
Foumban-Verification 2	**0.5; 0.75; 1; 1.5; 2.25**	
Bafoussam-Verification 1	**0.75; 1; 1.25; 1.5; 2.25**	**0.01; 0.5; 0.5; 0.75; 1; 1; 1.25; 1.5; 1.5; 2.25**
Bafoussam-Verification 2	**0.01; 0.5; 1; 1.25; 1.5**	
Bafoussam-Verification 3	**0.5; 0.75; 1; 1.5; 2.25**	**0.01;0.5; 1; 1; 1.25; 1.25; 1.5; 1.75; 2.25; 2.25**
Bafoussam-Verification 4	**1; 1.25; 1.5; 1.75; 2.25**	
Bafoussam-Verification 5	**0.01; 0.75; 1; 1.25; 2.25**	

[a]Used to replace LHZ code **0**, assuming that each class influences the modelling at some point

Lifetime of sites to rainfall-triggered landslide

Applying the Cobbs-Douglas formula, the following models were withdrawn from the analysis of variance, ANOVA, regressions on the five sites of landslides occurrence (Table 6).

These values were normalized by dividing each site S_i value by the mean of all values for each period. Then after, the most recurrent interval between LHZ codes, ***0.25***, was used to increment or decrement the normalized values towards the closest map class. Further, the means of the originally normalized values (Table 7) were computed for each S_i, giving 10 values for the study period 1948–2019. These means vary between ***0.009*** (Koutaba) and ***3.7*** (Njiloum2-Foumban) and served as coefficients for the kriging process to predict the verification sites S_0 (Table 7). In

Table 9 Observed sites kriging equations and results

Observed sites	Model	Values
S_0-*Foumban*	$-2.239 * 0.0348 + 0.026 * 3.711 + 0.485 * 1.026 + 0.001 * 0.009 + 2.468 * 0.219$	***1.06***
S_0-*Koutaba*	$1.863 * 0.0348 - 0.134 * 3.711 - 0.59 * 1.026 + 0.001 * 0.009 + 0.825 * 0.219$	***−0.8571***
S_0-*Bafoussam1*	$-2.988 * 0.0348 + 0.104 * 3.711 + 1.321 * 1.026 + 0.001 * 0.009 + 1.637 * 0.219$	***1.996***
S_0-*Bafoussam2*	$-1.507 * 0.0348 + 0.093 * 3.711 + 1.244 * 1.026 + 0.001 * 0.009 + 0.333 * 0.219$	***1.642***

Table 10 The Cox model parameters

	Start date	End date	Point date	Time (days)	Censored status	Covariate
S1-Njiloum1	1/1/1954	4/9/2018	1/8/2018	23,379	*1*	0.0348
S2-Njiloum2	1/1/1954	4/9/2018	1/8/2018	23,379	*1*	3.7114
S3-Njitout	1/1/1954	5/9/2018	1/8/2018	23,380	*1*	1.0257
S4-Koutaba	1/1/1954	23/10/2011	1/8/2018	20,871	*0*	0.009
S5-Gouache	1/1/1954	29/9/2019	1/8/2018	23,799	*1*	0.2189

addition, the nine verification sites S_0 were coupled in four dependent variables for the linear regression with the known sites S_i, and their LHZ codes were ordered in 10 value enhancing the variability, such as: *i)Foumban*: verification sites 1 and 2= S_0-**Foumban**; *ii) Koutaba*: verification sites 1 and 2= S_0-**Koutaba**; *iii) Bafoussam*: verification 1 and 2 = S_0-**Bafoussam1**, verification 3, 4 and 5= S_0-**Bafoussam2** (Table 8). Table 9 gives the four detailed kriging models for each S_0 as well as the results. With respectively ***1.99*** and ***1.642***, S_0-**Bafoussam1** and S_0-**Bafoussam2** are the highly exposed sites to a potential rainfall-triggered landslide. S_0-**Foumban** records the third value, ***1.06***, while S_0-**Koutaba**, shows the negative value – ***8571***.

Further, based on the landslide occurrence dates, the following parameters were introduced in the Cox model computation (Table 10).

The *start date* corresponds to the first landslide archived in Cameroon. The *end date* is the landslide occurrence events on the site. The "*point date*" is based on the analyst observations of the phenomenon, and in this case, it was defined according to the peak of rainfall starting in August, as well as on the highest percentage of landslide's occurrence that are *22%* in August, *45%* in September and *21%* in October (Table 2). The elapsed time was estimated in days rounded to the upper bound unit. The "*censored status"* is *1* for the failure to survive, that is the occurrence after the "*point date*" and *0* for success, i.e., the success or no-failure to survive before the "*point date*".

Table 11 Summary statistics

Total observed	Total failed	Total censored	Time steps	Covariate coefficient (β)	Hazard ratio
5	***4***	***1***	***4***	***0.388***	***1.474***

From the results presented in Fig. 13a, the survival probability of a site to rainfall-triggered landslide under *23,300* days of age was ***≈0.68*** (***68%***), and the site ***S4-Koutaba*** is the only concerned in this category. Between approximately *23,370* days and *23,700* days of ages, this probability was ***≈0.38*** (***38%***). The three sites ***S1-Njiloum1***, ***S2-Njiloum2*** and ***S3-Njitout*** in Foumban, belong to this interval. Above *23,700* days of age, the survival probability keeps decreasing between ***≈0.38*** and ***≈0.1*** (***10%***). The only site that matches this category is ***S5-Gouache*** in Bafoussam.

Inversely, and based on Fig. 13b, the rainfall-triggered landslides hazard increases with time. Technically then, the exposure of ***S5-Bafoussam*** to that hazard is higher than the other sites, while the lowest exposure is at ***S4- Koutaba***. The hazard ratio is ***1.474 ≈ 1.5***. (Table 11), corresponding to the time-to-event, meaning that at any time, one-and-half as many sites of occurrence (i.e., $\mathbf{1.5 * 5 = 7.5}$) are exposed to landslides.

The results above commented and their beta coefficients, $\boldsymbol{\beta = 0.388}$, were used to elaborate Cox

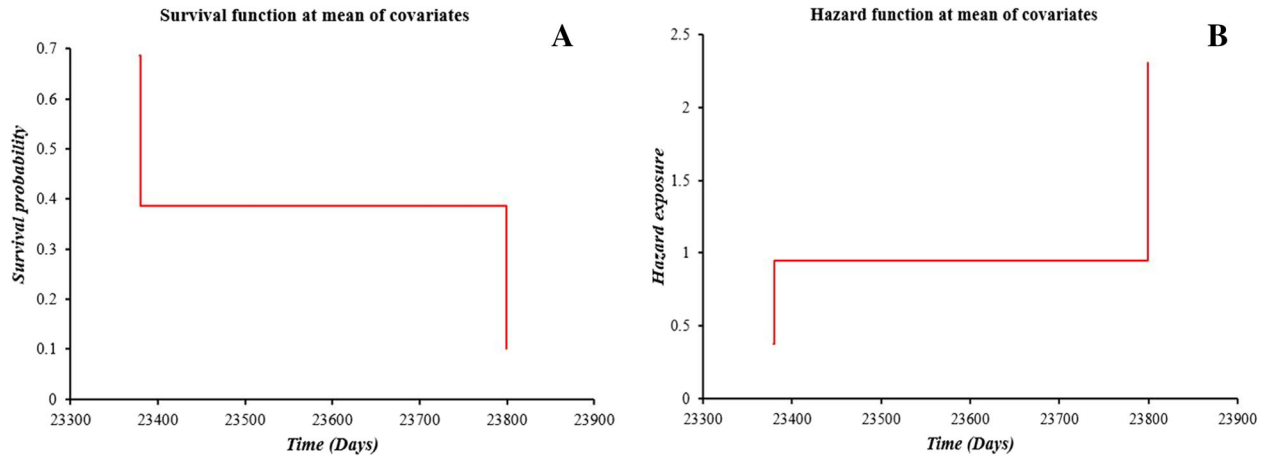

Fig. 13 Survival probability (**A**) and hazard exposure (**B**) of the five landslide occurrence sites

Table 12 Hazard ratios instantaneous risk models for the observed sites

Observed sites	Model	Values
S_0-*Foumban*	*exp*(0.388 ∗ 1.06)/ *exp* (0.388 ∗ 1)	***1.02***
S_0-*Koutaba*	*exp*(0.388 ∗ (−0.8571)/ *exp* (0.388 ∗ 1)	***0.49***
S_0-*Bafoussam1*	*exp*(0.388 ∗ 1.996)/ *exp* (0.388 ∗ 1)	***1.47***
S_0-*Bafoussam2*	*exp*(0.388 ∗ 1.642)/ *exp* (0.388 ∗ 1)	***1.28***

proportional hazards model for the four unknown sites, S_0. Their hazard ratio instantaneous risk was computed using the models detailed in Table 12 below.

The highest ratio is observed at S_0-*Bafoussam1* with ***1.47*** that is almost as same as the hazard ratio. The other sites in the decreasing order are S_0-*Bafoussam2*, S_0-*Foumban* and S_0-*Koutaba*, with respectively ***1.28***, ***1.02*** and ***0.49***.

Accuracies assessment and caveats

The two algorithms of SLIP and DRIP such as originally developed (Fayne et al., 2019) and adapted in this research connect landslides occurrence and huge rainfall. The interest has been to adjust the process to gaps in data, precisely the discontinuity among satellite images due to cloud cover and the unavailability of rainfall data at an hourly pace.

According to the SLIP processing, the highly exposed class to landslide occurrence meets the three conditions of bare soil, soil moisture and slope inclination thresholds, i.e., the LHZ code ***2.25***. Based on their location, five landslide sites match or are closely surrounded by this class, confirming the efficiency of the mapping method. In addition, five out of nine (*5/9*) verification sites support this statement, and give with the five previous a total match up to ***71%*** (*10/14* sites). Nonetheless, these accuracies are affected by the satellite images season, because the areas calculated may be *x time* more or less referring to the appending processing applied to approximate vegetation versus no-vegetation area between the dry and the rainy season (Appendix 2). In addition, the built-up extent and material can introduce biases especially when computing soil spectral indices (Ngandam et al., 2019). For instance, cities as Bafoussam and Foumban are characterized by their mi-rural/mid-urban patterns that include many houses in raw material such as earthen bricks and straw roofs, or unpaved dusty/muddy roads and tracks. Therefore, their reflectance may create mixed-pixel in the INDVI result, because they usually reflect enough in the red and SWIR wavelengths of Landsat 8 images just as the landslide-affected areas (Ngandam et al., 2019). Further, the DRIP modelling accuracy assessment holds in two approaches. Taking the confusion matrix extracted from the logistic modelling classification table, and with *50* observations of rainfall in the 10 zones, the *TPR* or sensitivity is up to *100%* (39/39), while the *FPR* or specificity is *82%* (Table 13). Both give an overall accuracy of *96%*, corresponding to the rate of rainfall and days of rainfall frequencies equal or beyond thresholds triggering the landslides.

Table 13 Classification table for the training sample – variable Y_1

Calculated / ***Observed***	***0***	***1***	***Total***	***%Correct***
0	9	2	11	***81.82***
1	0	39	39	***100***
Total	***9***	***41***	***50***	***96***

In addition, from the data of Table 13 above, the PPV is ***95%*** (39/41) while reversely, the NPV is ***5%*** (2/41). These are high accuracies of the efficiency of a post-landslide analysis in relation with a daily rainfall, to potentially know a date of occurrence. However, the unavailability of hourly rainfall to proceed to a timing limits to properly correlate the two data frequency.

On the last step dedicated to the survival analysis of sites, the goal was to predict and correlate daily rainfall, days of rainfall and the magnitude of the landslide in terms of speed of occurrence, to complete the status mapping and timely retrospective of the original algorithms. Based on the rainfall intensity deducted on a daily pace, the processing was able to perform a lifetime analysis, departing from the first event archived in Cameroon on *1/1/1954*, for the known and unknown sites. The survival probability of affected sites decreases with time, while the hazard of rainfall-triggered landslide increases. The unknown sites Cox's proportional hazards model can then be applied to the other sites of Cameroon, where rainfall data are available and landslides historic are archived. However, the huge rainfall of 81 mm in approximately 36 h preceding the landslide of Bafoussam-Gouache was not especially integrated in the processing, what raises the interrogation on the accurate timing as well as the rainfall intensity threshold to be used in the model.

Conclusion

The goal of this paper was to propose a derivative SLIP/DRIP procedure, adapted to countries and world's areas facing issues such as, satellite images important and a permanent cloud cover, poor spatial

Appendix 1

Table 14 Information on Landsat 8 images used (https://earthexplorer.usgs.gov)

Year	*Months*	*IDs*	*Center time*
2014	March	"LC81860562014080LGN01"	09:32:50
	December	"LC81860562014352LGN01"	09:32:33
2015	January	"LC81860562015019LGN01"	09:32:25
	December	"LC81860562015355LGN01"	09:32:34
2016	January	"LC81860562016006LGN02"	09:32:30
	December	"LC81860562016358LGN03"	09:32:40
2017	February	"LC81860562017056LGN00"	09:32:19
	December	"LC81860562017360LGN00"	09:32:37
2018	January	"LC81860562018027LGN00"	09:32:22
	December	"LC81860562018347LGN00"	09:32:18
2019	January	"LC81860562019014LGN00"	09:32:16
	June	"LC81860562019174LGN00"	09:32:18
	December	"LC81860562019350LGN00"	09:32:43

and temporal records of rainfall data for hourly or daily paces, or the lack of landslide inventories, all that impede the implementation of the robust SLIP/DRIP algorithms. Clearly thus, the proposed methodology did not pretend to substitute the standardized SLIP and DRIP algorithms. This approach is just another entry to these two algorithms, as an alternative to data voids, with the complementary step of survival analysis. To sum up, the *ante* and *post* landslide status of the affected areas approximately mapped, the rainfall threshold that triggers the landslide were modeled/estimated, and warning thresholds for a potential upcoming landslide were predicted for unknown sites based on survival probability and/or hazard exposure of known ones. Nevertheless, and logically, the accuracies of the outcomes suffered drawbacks and caveats, related to the accuracy of the areas affected by landslide, an efficiency of monitoring exposed areas in a window of 16 days with free Landsat 8 images, and the exact timing of the landslide occurrence in relation with the triggering rainfall.

Appendix 2

Image classification and NDVI computation for LULC extent assessment

Because all the cloud-free satellite images of the study area are only available for the dry season, there is a need of matching the land use land cover (LULC) areas with the rainy season when landslides always take place. Then, an image of the rainy season was used from 23 June 2019, and a cloud-free subset was extracted on the natural land covers area, i.e., vegetation and soil, and a supervised classification was performed for each image. Their average overall accuracy is *92%* and the average kappa coefficient is *0.89*. An image difference was then performed with the newest image (dry season) classification of the same year. The transformational technique that produces a change image from which a *change/no*

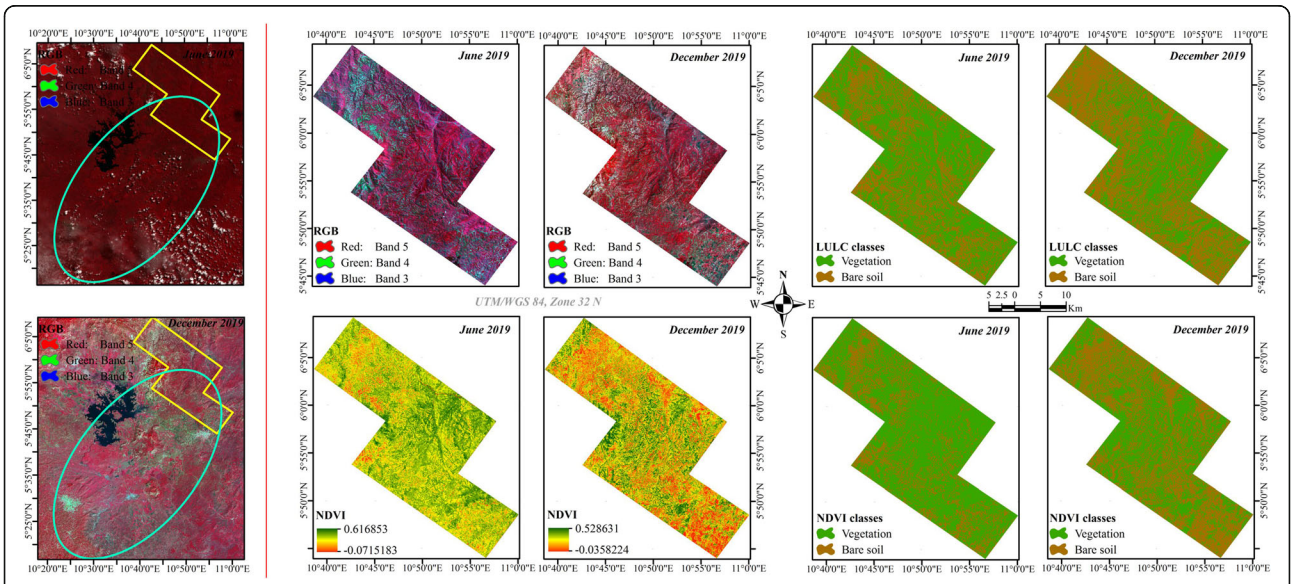

Fig. 14 Subsets of land cover extent approximation

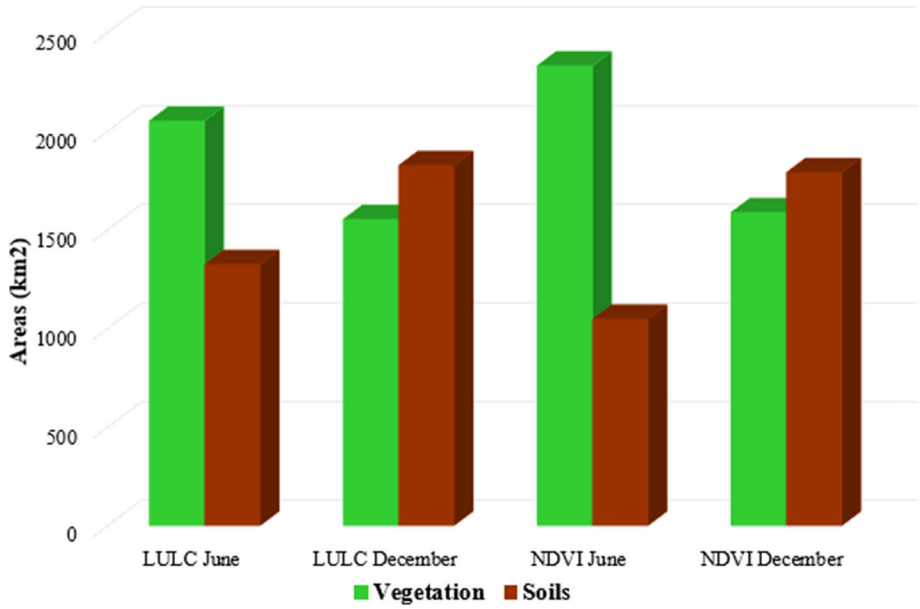

Fig. 15 Land Use Land Cover (LULC) – comparison for the classification and the NDVI

change threshold must be established was used. It is expressed as a symmetric relative difference in the following equation (Erdas, 2008):

$$\mathbf{Va} = \frac{T_2 - T_1}{|T_1|} + \frac{T_2 - T_1}{|T_2|} \quad (23)$$

Where **Va** is the new vegetation area and T is the time season image. It was noticed that in June, the 337,845 ha of the classification subset were occupied by the vegetation up to *61%* (205,295 ha) versus *39%* (132,550 ha) for soils, while in December, these percentages switch to *46%* (155,260 ha) for vegetation and *54%* (182,587 ha) for soils. To confirm the objects extraction and the trends above, the Normalized Difference Vegetation Index (NDVI) was computed for the two images (Fig. 14).

Statistics give *69%* (233,113 ha) for vegetation and *31%* (104,732 ha) for soil in June, versus *47%* (158,787 ha) for vegetation and *53%* (179,058 ha) for soil in December (Fig. 15). The average percentages are *65%* for vegetation and *35%* for soils in June, versus *46.5%* for vegetation

Appendix 3

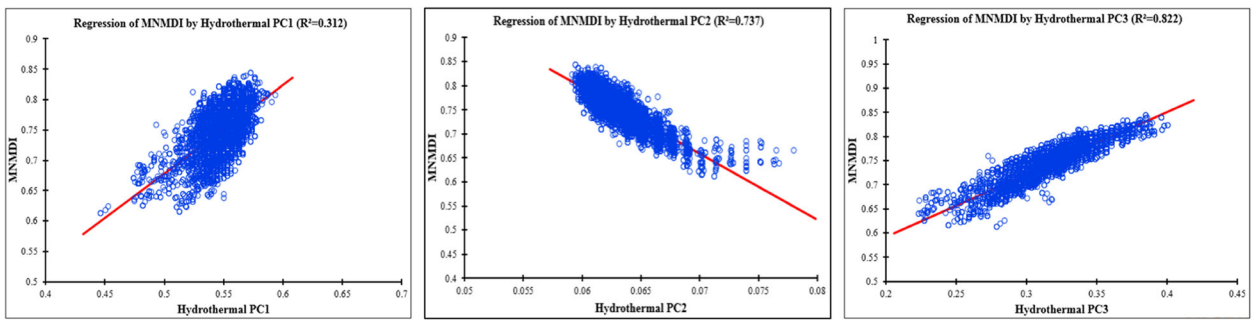

Fig. 16 Regression of MNMDI and Hydrothermal principal components bands

Appendix 4

Table 15 Rainfall data for 1948–2018 (Orange) and 2019 (Green)

	Zone 1		Zone 2		Zone 3		Zone 4		Zone 5		Zone 6		Zone 7		Zone 8		Zone 9		Zone 10	
	R	*D*	*R*	*D*	*R*	*D*	*R*	*D*	*R*	*D*	*R*	*D*	*R*	*D*	*R*	*D*	*R*	*D*	*R*	*D*
Jun.	350	27	350	25	352	28	352	25	369	25	361	25	377	25	389	24	358	24	369	25
Jul.	550	24	555	26	554	24	577	24	609	26	587	25	618	27	573	26	590	25	612	25
Aug.	617	25	620	25	648	25	650	26	654	28	658	28	688	29	687	31	679	30	692	27
Sept.	592	28	600	28	590	26	611	28	625	28	600	28	589	29	644	29	666	30	617	30
Oct.	378	26	377	26	392	23	379	25	391	24	398	24	395	23	412	23	445	25	400	24
Jun.	363	24	360	24	355	24	360	26	355	24	358	25	377	25	374	25	370	24	370	24
Jul.	546	25	583	25	535	24	579	24	579	26	600	26	557	27	548	28	571	25	577	25
Aug.	613	28	615	28	630	28	642	28	637	29	641	29	688	30	669	30	643	29	690	29
Sept.	597	30	580	28	581	28	594	28	618	30	617	30	615	29	644	29	621	30	633	29
Oct.	372	24	379	20	381	20	377	19	374	19	377	20	395	20	393	21	392	21	404	24

R=rainfall in millimeters and D=rainy days.

R = rainfall in millimeters and D = rainy days

and *53.5%* for soils in December. The ratios of the rainy season over the dry season areas were computed, showing that the rainy season vegetation area is about ***1.4*** times bigger than in dry season. Assuming that the average percentages could have the same influence on the classification process, the ratio of vegetation extent (*65%*) over the classification accuracy (*92%*) was calculated. The result obtained, i.e., ***0.598 ≈ 0.6***, was summed with the previous value, ***1.4***, as the best vegetation extent approximation for the rainy season, i.e., ***2*** times the vegetation area of the dry season's area. The ArcGISPro software expand function tool is useful for this purpose. In its principle, the class value targeted is multiplied by an *x* factor (***2*** here) to approximate the area as needed. The algorithm is written as:

$$\boldsymbol{Expand}\ (\boldsymbol{in\_raster}, \boldsymbol{number\_cells}, \boldsymbol{zone\_values}) \tag{24}$$

With *in_raster* representing the reclassified raster image, *number_cells* being the *x* factor and *zone_values* standing for the class to be expanded.

Acknowledgements
In memory of the 45 deaths and dozens of other victims (injured, homeless) reported for the 28 October 2019 landslide event in Bafoussam. In support of Cameroon's government, NGOs and civil groups action for predicting geohazards occurrence as well as mitigating their impact. The authors are grateful to the reviewers whose insightful remarks and suggestions were fundamental to the improvement of the manuscript.

Authors' contributions
The first and the second authors conceived, carried out the research and mapping, drafted the manuscript and finalized the corrections. The first and the third authors directed and validated the statistical analysis and modelling. All the authors contributed to fieldwork, data collection and curation, method validation, literature sourcing, mapping, editing, structuring and critical reviewing. All the authors read and approved the final manuscript.

Funding
The private consulting firm StatsN'Maps, through its *'Research Support Funds'* (SN'M-RSF), financially supported the purchase of articles and books chapters not free, as well as all the fieldwork investigations concerning rainfall data acquisition. The licenses of Erdas Imagine 2020 version 16.6.0.1366, ArcGisPro version 2.5 and XLStats 2020.1.64570 software used in this research are properties of StatsN'Maps and available upon request.

Availability of data and materials
All the data and material used for this research were incorporated as needed to the text or added as appendixes. Landsat 8 and DEM/SRTM images are freely available on *https://earthexplorer.usgs.gov//*. For all other detailed data and processing, contact the corresponding author via the following email: *stats.n.maps.expertise@gmail.com*.

Declarations

Competing interests
The authors declare that they have no competing interests.

Author details
[1]StatsN'Maps, Private Consulting Firm, Dallas, TX, USA. [2]Department of Geography, University of Yaoundé I, Yaoundé, Cameroon. [3]Institute of Mining and Geological Research, Yaoundé, Cameroon. [4]Department of Statistics and econometrics, University of Toulouse Capitol 1, Toulouse, France. [5]Geoscience, Water and Environment Laboratory, Faculty of Sciences, Mohammed V University in Rabat, Ibn Batouta Av., Rabat, Morocco. [6]Erik Jonsson School of Engineering and Computer Science, University of Texas in Dallas, Richardson, TX 75080, USA. [7]Department of Geography, University of Aix Marseille, Marseille, France.

Received: 11 March 2020 Accepted: 9 June 2021
Published online: 30 July 2021

References

Ada M, San BT (2018) Comparison of machine-learning techniques for landslide susceptibility mapping using two-level random sampling (2LRS) in Alakir catchment area, Antalya, Turkey. Nat Hazards 90(1):237–263. https://doi.org/10.1007/s11069-017-3043-8

Anbalagan R, Kumar R, Lakshmanan K, Parida S, Neethu S (2015) Landslide hazard zonation mapping using frequency ratio and fuzzy logic approach, a case study of Lachung Valley, Sikkim. Geoenviron Disast 2(6):1–17. https://doi.org/10.1186/s40677-014-0009-y

Atkinson PM, Massari R 1998. Generalised linear modelling of susceptibility to landsliding in the central Apennines, Italy. Computers and Geosciences, (24), 4,373–385

Ayonghe SN, Suh CE, Ntasin EB, Samalang P, Fantong W (2002) Hydrologcally, seismically and tectonically triggered landslides along the Cameroon volcanic line, Cameroon. Afr Geosci Rev 9(4):325–335

Balla A, Kagou Dongmo A, Nkouathio DG, Ngapgue F (2013) Land instability in the highlands of western Cameroon: geological and geotechnical characterization of the Kekem landslide. Bull de l'Institut Sci 35:39–51

Baudains P, Zamazalová S, Altaweel M, Wilson A (2015) Modeling strategic decisions in the formation of the early neo-Assyrian empire. Cliodynamics 6(1):1–23. https://doi.org/10.21237/C7clio6125390

Blahut J, Van Westen C, Sterlacchini S (2010) Analysis of landslide inventories for accurate prediction of debris-flow source areas. Geophys J R Astron Soc 119(1-2):36–51. https://doi.org/10.1016/j.geomorph.2010.02.017

Brabb, E. 1993. Proposal for worldwide landslide hazard maps. In Novosad, S. & Wagner, P. (eds.), Proceedings of the 7th International Conference and Workshop on Landslides, 15–27. https://pubs.er.usgs.gov/publication/70197564

Braun SA (2011) TRMM Status. In: 7th GPM international planning workshop, Tokyo http://www.eorc.jaxa.jp/GPM/ws7/pdf/5thDEC2007/AM/5_am06.pdf

Brusden D (1984) Mudslides. In: Brusden D, Prior D (eds) Slope Instability. Wiley, Chichester, UK, pp 363–418.

Bui D, Pradhan B, Lofman O, Dick O (2012) Landslide susceptibility assessment in the Hoa Binh Province of Vietnam: a comparison of the Levenberg-Marquardt and Bayesian regularized neural networks. Geophys J R Astron Soc 171–172:12–29. https://doi.org/10.1016/j.geomorph.2012.04.023

Calvello M, Cascini L, Mastroianni S (2013) Landslide zoning over large areas from a sample inventory by means of scale-dependent terrain units. Geophys J R Astron Soc 182:33–48. https://doi.org/10.1016/j.geomorph.2012.10.026

Canavesi V, Segoni S, Rosi A, Ting X, Nery T, Catani F, Casagli N (2020) Different approaches to use morphometric attributes in landslide susceptibility mapping based on Meso-scale spatial units: a case study in Rio de Janeiro (Brazil). Remote Sens 12(11):1826. https://doi.org/10.3390/rs12111826

Colombo A, Lanteri L, Ramasco M, Troisi C (2005) Systematic GIS-based landslide inventory as the first step for effective landslide-hazard management. Landslides 2(4):291–301. https://doi.org/10.1007/s10346-005-0025-9

Couture R (2011) Landslide terminology - National Technical Guidelines and best practices on landslides. Geol Survey Can Open File 6824:12

Cox DR (1972) Regression models and life-tables. J R Stat Soc 34(2):187–220 https://www.jstor.org/stable/2985181

Crozier MJ (1986) Landslides: Causes, Consequences and Environment. Croom Helm Limited, London and Sidney, p 252

Cruden DM (1991) A simple definition of landslide. Bull Int Assoc Eng Geol 43(1): 27–29. https://doi.org/10.1007/BF02590167

Cruden DM, Varnes DJ (1996) Landslide types and processes. Transportation Research Board, U.S. Nat Acad Sci 247:36–75 http://pubs.usgs.gov/fs/2004/3072/

Cyr D, Gauthier S, Bergeron Y (2007) Scale-dependent determinants of heterogeneity in fire frequency in a coniferous boreal forest of eastern Canada. Landsc Ecol 22(9):1325–1339. https://doi.org/10.1007/s10980-007-9109-3

Dahal BK, Dahal RK (2017) Landslide hazard map: tool for optimization of low-cost mitigation. Geoenviron Disast 4(8):1–9. https://doi.org/10.1186/s40677-017-0071-3

Dezfuli AK, Ichoku CM, Mohr KI, Huffman GJ (2017) Precipitation characteristics in west and East Africa from satellite and in situ observations. J Hydrometeorol 18(6):1799–1805. https://doi.org/10.1175/JHM-D-17-0068.1

Djouka FML, Schulz B, Schüssler U, Tchouankoue JP, Nzolang C (2008) Geochemistry of the Bafoussam Pan-African I- and S-type granitoids in western Cameroon. J Afr Earth Sci 50(2-4):148–167. https://doi.org/10.1016/j.jafrearsci.2007.09.015

Elsheikh AA, Gao SS, Liu KH (2014) Formation of the Cameroon volcanic line by lithospheric basal erosion: insight from mantle seismic anisotropy. J Afr Earth Sci 100:96–108. https://doi.org/10.1016/j.jafrearsci.2014.06.011

Erdas Imagine (2008) Imagine DeltaCue user's guide. ERDAS INC., p 128 http://faculty.une.edu/cas/szeeman/rs/docs/DeltaCue.pdf

Fayne JV, Ahamed A, Roberts-Pierel J, Rumsey AC, Kirschbaum DB (2019) Automated satellite-based landslide identification product for Nepal. Earth Interact 23(3):23–21. https://doi.org/10.1175/EI-D-17-0022.1

Galli M, Ardizzone F, Cardinali M, Guzzetti F, Reichenbach P (2008) Comparing landslide inventory maps. Geomorphology 94(3-4):268–289. https://doi.org/10.1016/j.geomorph.2006.09.023

Garosi Y, Sheklabadi M, Pourghasemi HR, Besalatpour AA, Conoscenti C, Oost KV (2018) Comparison of differences in resolution and sources of controlling factors for gully erosion susceptibility mapping. Geoderma 330:65–78. https://doi.org/10.1016/j.geoderma.2018.05.027

Goetz J, Brenning A, Petschko H, Leopold P (2015) Evaluating machine learning and statistical prediction techniques for landslide susceptibility modeling. Comput Geosci 81:1–11. https://doi.org/10.1016/j.cageo.2015.04.007

Gosh K, Bandyopadhyay S, Kumar De S (2011) A comparative evaluation of weight-rating and analytical hierarchical (AHP) for landslide susceptibility mapping in Dhalai District, Tripura. Environ Earth J Observ:175–193. https://doi.org/10.1007/978-3-319-46010-9_12

Guzzetti F, Carrara A, Cardinali M, Reichenbach P (1999) Landslide hazard evaluation: a review of current techniques and their application in a multi-scale study, Central Italy. Geomorphology 31(1-4):181–216. https://doi.org/10.1016/S0169-555X(99)00078-1. https://fr.climate-data.org/afrique/cameroun/west-1367/. https://weather-and-climate.com/average-monthly-Rainfall-Temperature-Sunshine

Guzzetti F, Reichenbach P, Cardinali M, Galli M, Ardizzone F (2005) Probabilistic landslide hazard assessment at the basin scale. Geomorphology 72(1-4):272–299. https://doi.org/10.1016/j.geomorph.2005.06.002

Hutchinson, J.N. 1988. General Report: Morphological and geotechnical parameters of landslides in relation to geology and hydrogeology. Proceedings of the Fifth International Symposium on Landslides, Bonnard, C. (Eds.). https://doi.org/10.1016/0148-9062(89)90310-0, 26, 2, 88

Institute of Geological and Mining Research (IGMR), Kankeu B, Ntchantcho R (2019) Natural disaster of Gouache-Bafoussam (West-Cameroon), scientific causes. In: Fieldwork mission report, Translated from original version in French, p 14

Institute of Geological and Mining Research (IGMR), Penaye J, Ateba B, Wokwenmendam Nguet P, Moudioh C (2018) Disaster of September 2018 in the Njintout and Njiloum districts of Foumban town (West-Cameroon): Scientific opinion. In: Fieldwork mission report, Translated from original version in French, p 15

Jiménez-Perálvarez JD, Irigaray C, El Hamdouni R, Chacón J (2011) Landslide-susceptibility mapping in a semi-arid mountain environment: an example from the southern slopes of Sierra Nevada (Granada, Spain). Bull Eng Geol Environ 70(2):265–277. https://doi.org/10.1007/s10064-010-0332-9

Kanungo D, Arrora M, Sarkar S, Gupta R (2009) Landslide susceptibility zonation (LSZ) mapping-a review. J South Asian Disast Stud 2:81–105

Kanungo DP, Arora MK, Sarkar S, Gupta RP (2006) A comparative study of conventional, ANN black box, fuzzy and combined neural and fuzzy weighting procedures for landslide susceptibility zonation in Darjeeling Himalayas. Eng Geol 85(3–4):347–366. https://doi.org/10.1016/j.enggeo.2006.03.004

Kayastha P, Dhital M, De Smedt F (2013) Application of the analytical hierarchy process (AHP) for landslide susceptibility mapping: a case study from the Tinau watershed, West Nepal. Comput Geosci 52:398–408. https://doi.org/10.1016/j.cageo.2012.11.003

Kirschbaum DB, Adler R, Hong Y, Lerner-Lam A (2009) Evaluation of a satellite-based landslide algorithm using global landslide inventories. Nat Hazards Earth Syst Sci 9(3): 673–686. https://doi.org/10.5194/nhess-9-673-2009

Klein CA (2009) Characteristic strength, Weibull modulus, and failure probability of fused silica glass. Opt Eng 48(11):113401. https://doi.org/10.1117/1.3265716

Komac M (2006) A landslide susceptibility model using the analytical hierarchy process method and multivariate statistics in perialpine Slovenia. Geomorphology 74(1):17–28. https://doi.org/10.1016/j.geomorph.2005.07.005

Lee C, Huang C, Lee J, Pan K, Lin M, Dong J (2008) Statistical approach to storm event-induced landslides susceptibility. Nat Hazards Earth Syst Sci 8(4):941–960. https://doi.org/10.5194/nhess-8-941-2008

Lee S (2005) Application of logistic regression model and its validation for landslide susceptibility mapping using GIS and remote sensing data. Int J Remote Sens 7(7):1477–1491. https://doi.org/10.1080/01431160412331331012

Lin L, Lin Q, Wang Y (2017) Landslide susceptibility mapping on a global scale using the method of logistic regression. Nat Hazards Earth Syst Sci 17(8): 1411–1424. https://doi.org/10.5194/nhess-17-1411

Maidment RI, Grimes D, Allan RP, Tarnavsky E, Stringer M, Hewison T, Roebeling R, Black E (2014) The 30 years TAMSAT African rainfall climatology and time series (TARCAT) dataset. J Geophys Res 119(18):10619–10644. https://doi.org/10.1002/2014JD021927

Marjanovi'c, M., Kova˘cevi'c, M., Bajat, B., Voženílek, V. (2011) Landslide susceptibility assessment using SVM machine learning algorithm. Eng Geol 123(3):225–234. https://doi.org/10.1016/j.enggeo.2011.09.006

Martha T, Van Westen C, Kerle N, Jetten V, Vinod Kumar K (2013) Landslide hazard and risk assessment using semi-automatically created landslide inventories. Geophys J R Astron Soc 184:139–150. https://doi.org/10.1016/j.geomorph.2012.12.001

Meena SR, Ghorbanzadeh O, Blaschke T (2019) A comparative study of statistics-based landslide susceptibility models: a case study of the region affected by the Gorkha earthquake in Nepal. Int J Geo-Inform 8(2):94. https://doi.org/10.3390/ijgi8020094

Meten M, Bhandary PN, Yatabe R (2015) Effect of landslide factor combinations on the prediction accuracy of landslide susceptibility maps in the Blue Nile gorge of Central Ethiopia. Geoenviron Disast 2(9):1–17. https://doi.org/10.1186/s40677-015-0016-7

Moundi A, Konfor Njilah I, Ghogomou Tanwi R, Wokwenmendam Nguet P (2008) New geochronological data for the continental alkaline flood basalts of the Bamoun plateau (West Cameroon): evidence for an early alkaline volcanism of the Cameroon volcanic line. Disast Adv 1(3):27–33

Moundi A, Wandji P, Bardintzeff J-M, Ménard J-J, Atouba Okomo LC, Mouncherou OF, Reusser E, Bellon H, Tchoua FM (2007) Les basaltes éocènes à affinité transitionnelle du plateau Bamoun, témoins d'un réservoir mantellique enrichi sous la Ligne Volcanique du Cameroun. C R Geosci 339(6):396–406. https://doi.org/10.1016/j.crte.2007.04.001

Nam K, Wang F (2020) An extreme rainfall-induced landslide susceptibility assessment using autoencoder combined with random forest in Shimane prefecture, Japan. Geoenviron Disast 7(6):1–16. https://doi.org/10.1186/s40677-020-0143-7

Ngandam Mfondoum AH, Gbetkom PG, Wokwenmendam Nguet P, Cooper R, Hakdaoui S (2019) Assessing the spatial metabolism of a mid-urban/mid-rural city: the relationship built-up, vegetation, bare soil and urban heat in Foumban (west-Cameroon, Central Africa) - periods 1987–2003 - 2019. Third International Land Use Symposium, ILUS, Paris, pp 4–6. https://doi.org/10.13140/RG.2.2.13421.33766

Ngongang NB, Kamgang P, Chazot G, Agranier A, Bellon B, Nonnotte P (2015) Age, geochemical characteristics and petrogenesis of Cenozoic intraplate alkaline volcanic rocks in the Bafang region, West Cameroon. J Afr Earth Sci 102:218–232. https://doi.org/10.1016/j.jafrearsci.2014.10.011

Njilah IK (1991) Geochemistry and Petrogenesis of Tertiary-Quaternary volcanic rocks from Oku-Ndu area, N.W. PhD Thesis, University of Leeds, Cameroon, p 350

Njonfang E, Moreau C, Tchoua FM (1998) The Foumban-Bankim mylonitic band, West-Cameroon. A HT-MP shear zone. Comptes Rendus de l'Académie des Sciences 327(11):735–741. https://doi.org/10.1016/S1251-8050(99)80044-5

Pardeshi SD, Autade SE, Pardeshi SD (2013) Landslide hazard assessment: recent trends and techniques. Springer Plus 2(1):523. https://doi.org/10.1186/2193-1801-2-523

Petley D (2012) Global patterns of loss of life from landslides. Geology 40(10): 927–930. https://doi.org/10.1130/G33217.1

Petley DN, Mantovani F, Bulmer MH, Zannoni A (2005) The use of surface monitoring data for the interpretation of landslide movement patterns. Geomorphology 66 (1-4):133–147

Pham BT, Bui DT, Prakash I, Dholakia M (2016b) Rotation forest fuzzy rule-based classifier ensemble for spatial prediction of landslides using GIS. Nat Hazards 83(1):97–127. https://doi.org/10.1007/s11069-016-2304-2

Pham BT, Pradhan B, Bui DT, Prakash I, Dholakia M (2016a) A comparative study of different machine learning methods for landslide susceptibility assessment: a case study of Uttarakhand area (India). Environ Model Software J 84:240–250. https://doi.org/10.1016/j.envsoft.2016.07.005

Pham BT, Prakash I, Bui DT (2018) Spatial prediction of landslides using a hybrid machine learning approach based on random subspace and classification and regression trees. Geomorphology 303:256–270. https://doi.org/10.1016/j.geomorph.2017.12.008

Pour BA, Hashim M 2014. Alteration mineral mapping using ETM+ and Hyperion remote sensing data at Bau Gold Field, Sarawak, Malaysia. Earth and Environment Science (18), 1–5.

Pradhan B, Lee S (2009) Landslide risk analysis using artificial neural network model focusing on different training sites. Int J Phys Sci 4(1):001–015

Preuth T, Glade T, Demoulin A (2010) Stability analysis of human-influenced landslides in eastern Belgium. Geomorphology 120(1-2):38–47. https://doi.org/10.1016/j.geomorph.2009.09.013

Roy J, Saha S (2019) Landslide susceptibility mapping using knowledge driven statistical models in Darjeeling District, West Bengal, India. Geoenviron Disast 6(11):1–18. https://doi.org/10.1186/s40677-019-0126-8

Sarkar S, Kanungo D, Patra A, Kumar P (2006) Disaster mitigation of debris flows, slope failures and landslides. GIS based landslide susceptibility mapping- a case study in Indian Himalaya. Universal Academy Press, pp 617–624

Sharma S, Mahajan AK (2018) Comparative evaluation of GIS-based landslide susceptibility mapping using statistical and heuristic approach for Dharamshala region of Kangra Valley, India. Geoenviron Disast 5(4):1–16. https://doi.org/10.1186/s40677-018-0097-1

Shirzadi A, Soliamani K, Habibnejhad M, Kavian A, Chapi K, Shahabi H, Chen W, Khosravi K, Thai Pham B, Pradhan B, Ahmad A, Bin Ahmad B, Tien Bui D (2018) Novel GIS based machine learning algorithms for shallow landslide susceptibility mapping. Sensors 18(11):3777. https://doi.org/10.3390/s18113777

Singh C, Behra K, Rocky W (2011) Landslide susceptibility along NH-39 between Karong and Mao, Senapati District, Manipur. J Geol Soc India 78(6):559–570. https://doi.org/10.1007/s12594-011-0120-6

Tchindjang M (2012) Paradoxes and risks in Cameroons' highlands: natural multifonctionality and human undervaluation, vol 7. HDR, University of Paris, p 266 Translated from the original version in French

Tchindjang M (2013) Mapping of natural hazards in Cameroon. International Cartographic Association https://icaci.org/files/documents/ICC.../403_proceeding.pdf

Tofani V, Segoni S, Agostini A, Catani F, Casagli N (2013) Technical note: use of remote sensing for landslide studies in Europe. Nat Hazards Earth Syst Sci 13(2):299–309. https://doi.org/10.5194/nhess-13-299-2013

United Nation Office for Disaster Risk Reduction –UNISDR (2017) In: Sassa K et al (eds) UNISDR'S contribution to science and technology for disaster rick reduction and the role of the international consortium on landslides (ICL), pp 109–115

USGS (2004) Landslides types and processes, p 4 https://pubs.usgs.gov/fs/2004/3072/pdf/fs2004-3072.pdf

Van Westen CJ, Seijmonsbergen AC, Mantovani F (1999) Comparing landslide hazard maps. Nat Hazards 20(2–3):137–158. https://doi.org/10.1023/A:1008036810401

Varnes DJ (1958) Landslide types and processes. Landslide Eng Pract 29:20–47 http://onlinepubs.trb.org/Onlinepubs/sr/sr29/29-003.pdf

Varnes DJ (1978) Slope movement types and processes. Landslide 176:20–47 http://onlinepubs.trb.org/Onlinepubs/sr/sr176/176-002.pdf

Varnes DJ (1984) Landslide Hazard zonation—a review of principles and practice. IAEG – UNESCO, Commission on Landslides, pp 1–6 http://worldcat.org/isbn/9231018957

Wang H, Sassa K (2005) Comparative evaluation of landslide susceptibility in Minamata area. Japan Environ Geol 47(7):956–966. https://doi.org/10.1007/s00254-005-1225-2

Wang L, Qu J (2007) NMDI: a normalized multi-band drought index for monitoring soil and vegetation moisture with satellite remote sensing. Geophys Res Lett 34(20):L20405. https://doi.org/10.1029/2007GL031021

Wokwenmendam Nguet P (2019) Petrography, geochemistry and geochronology of Nana complex (Tikar plain): geodynamic and metallogenic implications. PhD dissertation, university of Yaoundé, Cameroon, Translated from the original version in French, p 243

World Landslide Forum-WLF (2017) Advancing culture of living with landslides, pp 109–115. https://doi.org/10.1007/978-3-319-59469-9

Wu Y, Li W, Liu P, Bai H, Wang Q, He J, Liu Y, Suns (2016) Application of analytic hierarchy process model for landslide susceptibility mapping in the Gangu country, Gangu province. Environ Earth Sci 75(5):422. https://doi.org/10.1007/s12665-015-5194-9

Xiao T, Segoni S, Chen L, Yin K, Casagli N (2020) A step beyond landslide susceptibility maps: a simple method to investigate and explain the different

outcomes obtained by different approaches. Landslides 17(3):627–640. https://doi.org/10.1007/s10346-019-01299-0
Xiong K, Adhikari BR, Stamatopoulos CA, Zhan Y, Wu S, Dong Z, Di B (2020) Comparison of different machine learning methods for debris flow susceptibility mapping: a case study in the Sichuan Province, China. Remote Sens 12(2):295. https://doi.org/10.3390/rs12020295
Yang H, Wang F, Miyajima M (2015) Investigation of shallow landslides triggered by heavy rainfall during typhoon Wipha (2013), Izu Oshima Island, Japan. Geoenviron Disast 2(15):1–10. https://doi.org/10.1186/s40677-015-0023-8
Yang H, Wang F, Vilimek V, Araiba K, Asano S (2012) Investigation of rainfall-induced shallow landslides on the northeastern rim of Aso caldera, Japan. Geoenviron Disast 2(20):1–14. https://doi.org/10.1186/s40677-015-0028-3
Zhao C, Lu Z (2018) Remote sensing of landslides–a review. Remote Sens 10(2): 279. https://doi.org/10.3390/rs10020279

Publisher's Note